An Interbacterial Cysteine Protease Toxin Inhibits Cell Growth by Targeting Type II DNA Topoisomerases GyrB and ParE

Pin-Yi Song[1,2,6], Chia-En Tsai[1,2,6], Yung-Chih Chen[2], Yu-Wen Huang[2], Po-Pang Chen[2,3], Tzu-Haw Wang[4], Chao-Yuan Hu[2], Po-Yin Chen[1,2], Chuan Ku[4,5], Kuo-Chiang Hsia[1,2,3], See-Yeun Ting[1,2,5,7†]

[1] Molecular and Cell Biology, Taiwan International Graduate Program, Academia Sinica and National Defense Medical Center, Taipei, 11490, Taiwan

[2] Institute of Molecular Biology, Academia Sinica, Taipei 11529, Taiwan

[3] Institute of Biochemistry and Molecular Biology, College of Life Sciences, National Yang Ming Chiao Tung University, Taipei 11221, Taiwan

[4] Institute of Plant and Microbial Biology, Academia Sinica, Taipei 115201, Taiwan

[5] Genome and Systems Biology Degree Program, National Taiwan University, Taipei 106319, Taiwan

[6] These authors contributed equally

[7] Lead contact

[†]Correspondence: syting@gate.sinica.edu.tw

Keywords:

Papain-like cysteine protease, Antibacterial toxin, DNA topoisomerase, Interbacterial antagonism

Abstract

Bacteria deploy a diverse arsenal of toxic effectors to antagonize competitors, profoundly influencing the composition of microbial communities. Previous studies have identified an interbacterial toxin predicted to exhibit proteolytic activity that is broadly distributed among Gram-negative bacteria. However, the precise mechanism of intoxication remains unresolved. Here, we demonstrate that one such protease toxin from *Escherichia coli*, Cpe1, disrupts DNA replication and chromosome segregation by cleaving conserved sequences within the ATPase domain of type II DNA topoisomerases GyrB and ParE. This cleavage effectively inhibits topoisomerase-mediated relaxation of supercoiled DNA, resulting in impaired bacterial growth. Cpe1 belongs to the papain-like cysteine protease family and is associated with toxin delivery pathways, including the type VI secretion system and contact-dependent growth inhibition. The structure of Cpe1 in complex with its immunity protein reveals a neutralization mechanism involving competitive substrate binding rather than active site occlusion, distinguishing it from previously characterized effector-immunity pairs. Our findings unveil a unique mode of interbacterial intoxication and provide insights into how bacteria protect themselves from self-poisoning by protease toxins.

Introduction

Bacteria in natural environments exist within complex communities, where interactions—both cooperative and antagonistic—are pivotal to their survival. A key aspect of bacterial competition is the acquisition of limited resources, which has driven the evolution of a wide array of interbacterial antagonistic mechanisms, including the production of antibiotics, antimicrobial peptides, and diffusible proteinaceous toxins[1,2]. More recently, sophisticated mechanisms for

45 distinguishing kin and antagonizing competitors have been identified[3-8]. Among these, Gram-
46 negative bacteria utilize specialized secretion systems, such as contact-dependent growth
47 inhibition (CDI), the type IV secretion system (T4SS), and the type VI secretion system (T6SS),
48 to translocate toxins into neighboring cells in a contact-dependent manner, whereas Gram-positive
49 bacteria rely on the Esx secretion system for similar antagonistic interactions[9]. These secretion
50 systems allow pathogenic bacteria to establish dominance in polymicrobial infections and enable
51 commensal bacteria to establish compatibility within microbial consortia[10-12].

52 Interbacterial toxins delivered via these systems enhance the competitive fitness of the
53 producing bacteria by inhibiting or killing competitors. Depending on their biochemical properties,
54 the impact of these effectors on target cells can vary considerably. For instance, a wide variety of
55 antibacterial toxins induce cell lysis by disrupting the cellular membrane or degrading cell wall
56 peptidoglycans[9,13-17]. Pore-forming toxins exert their toxicity by inserting themselves into the
57 cellular membrane and causing its depolarization[18-20]. Some toxins are translocated into the
58 cytoplasm, where they compromise DNA/RNA integrity or deplete the cellular energy resources
59 of target cells[21-26]. Post-translationally modified toxins have been found to target essential proteins
60 involved in bacterial cell division and protein synthesis[27-30]. This broad spectrum of targets allows
61 the toxins to act across phylogenetically diverse bacteria. Most of the intoxication mechanisms of
62 these antibacterial toxins are inherently indiscriminate. Therefore, bacteria encode specific
63 immunity proteins adjacent to their cognate toxin genes to prevent self-intoxication or harm to kin
64 cells. These immunity proteins typically neutralize toxins by occluding their active sites[31]. In some
65 cases, other neutralization mechanisms, such as enzymatic antagonism of effector activity or
66 structural disruption of the effector domain, have also been reported[27,32].

Although significant progress has been made in identifying novel interbacterial toxins in recent years, detailed characterizations of their intoxication mechanisms remain lacking[33-35]. For example, comparative genomic, advanced genetic screening, and structure-based searching approaches have uncovered novel effectors with conserved catalytic residues indicative of protease and peptide amidase activities, which inhibit bacterial growth during interbacterial competition[36-38]. However, their natural substrates and precise biochemical activities have yet to be elucidated. In this study, we describe an interbacterial toxin that targets the essential type II DNA topoisomerases GyrB and ParE via papain-like cysteine protease (PLCP) activity. This toxin is phylogenetically widespread and shares hallmarks of interbacterial effectors secreted via the T6SS and CDI pathways. Homologs of this toxin are similar to PLCPs associated with ATP-binding cassette (ABC) transporters involved in bacterial protein export. However, their role in interbacterial antagonism, specifically in targeting and damaging essential proteins, has not been elucidated. Interestingly, our structural analyses further reveal that protection against the PLCP toxins is conferred by cognate immunity proteins, which block substrate binding rather than occlude the active site, thereby inactivating the toxicity. Our findings not only expand our understanding of protease effectors in interbacterial conflict but also uncover a previously undescribed mode of immunity protection.

Results

Papain-like Cysteine Protease Antibacterial Effectors Are Found in Different Gram-negative Bacteria

Previous studies on T6SS–associated protease effectors, such as EvpQ from *Edwardsiella piscicida* and TsaP from *Escherichia coli*, have predicted their classification within the family of

90 PLCPs[36,37]. The defining feature of this protease family is a conserved catalytic triad, consisting
91 of a cysteine (Cys) thiol group, a histidine (His) imidazolium ring, and a third residue—either
92 aspartate (Asp) or asparagine (Asn)—that orients and activates the imidazolium ring for peptide
93 bond hydrolysis (**Figure 1a**). PLCPs in bacteria have been well characterized for their roles as
94 virulence factors in both animal and plant infections[39-41], as well as for functioning as maturation
95 proteases in a variety of ABC transporters, where they specifically recognize and cleave signal
96 peptides before substrate export[42-44]. However, their function as antibacterial toxins has yet to be
97 fully understood[33].

98 To explore the prevalence of PLCPs involved in interbacterial antagonism, we conducted
99 a homology search against the National Center for Biotechnology Information (NCBI) non-
100 redundant database using PSI-BLAST[45], employing the cysteine protease domains of EvpQ and
101 TsaP as queries[36,37]. Homologous genes with more than 10% sequence identity were retrieved, and
102 their gene neighborhoods were analyzed to infer potential roles in interbacterial competition. The
103 low sequence identity threshold was selected to ensure identification of both EvpQ- and TsaP-like
104 proteins. Consequently, we identified 155 unique genes encoding PLCP domains associated with
105 either the T6SS or CDI pathways. Of these, 70 were located at the C-terminus of T6SS toxin-
106 delivery proteins (*e.g.*, PAAR, VgrG, and Rhs)[46,47], and the remaining 85 were linked to the CdiA
107 carrier protein in the CDI pathway[48] (**Figure 1b, Supplementary Figure 1a,** and **Supplementary**
108 **Table 1**). Multiple sequence alignments of these homologs, along with representative PLCPs from
109 ABC transporters (*e.g.,* ComA and LahT), confirmed the presence of the conserved catalytic triad
110 (Cys, His, Asp/Asn)[49,50] (**Figure 1c**).

111 Phylogenetic analysis of the identified protease domain sequences revealed close
112 similarities to EvpQ and TsaP[36,37] (**Figure 1d** and **Supplementary Figure 2**). These toxin

homologs are distributed across Phylum Pseudomonadota, including in Alpha-, Beta-, Gamma-, and Delta-proteobacteria, and they are found in bacteria across a range of ecological niches, including within animal and insect hosts and in the environment. Additionally, fifteen T6SS–associated homologs were identified in distantly related phyla, such as Acidobacteriota, Actinomycetota, Chloroflexota, Cyanobacteria, and Myxococcota (**Figure 1d, Supplementary Figures 1-2,** and **Supplementary Table 1**). Although we detected no clear correlation between phylogeny, taxonomy, and toxin-delivery pathway, the phylogenetic similarity of these homologs from diverse phyla implies that horizontal gene transfer may have contributed to the evolutionary dissemination of PLCP toxins.

To prevent self-intoxication, toxin-producing bacteria carry immunity proteins, typically encoded adjacent to the toxin genes in the genome[31]. Consistent with this scenario, we found that the majority of the identified PLCP toxin genes are followed in the respective genomes by putative immunity genes (**Figure 1b** and **Supplementary Figure 1b**). The putative immunity proteins range from 79 to 239 amino acids and exhibit considerable sequence divergence, likely reflecting their specificity towards their cognate PLCP toxins. Supporting this idea, the sequence identity between each immunity gene and its corresponding PLCP toxin is positively correlated, evidencing their coevolutionary nature (**Supplementary Table 1**). Together, these findings suggest that PLCP toxins, along with their cognate immunity proteins, are found in various Gram-negative bacterial species. For clarity in this study, we have designated the identified PLCP toxin as Cpe1 (cysteine protease effector 1) and the cognate immunity protein as Cpi1 (**Figures 1b, d**).

The Structure of the Cpe1–Cpi1 Complex Reveals a Distinct Toxin-Neutralization Mechanism

136 Pioneering studies by Li *et al.* and Lu *et al*. have demonstrated that bacteria, such as *E.*
137 *piscicida* and *E. coli*, utilize T6SS–associated Cpe1 effectors to mediate interbacterial
138 antagonism[36,37]. However, the precise mechanisms underlying Cpe1-induced toxicity remain
139 unclear. To elucidate the mode of action of Cpe1, we employed structural biology approaches to
140 gain insights into its toxic activity. Notably, overexpression of the Cpe1 toxin domain ($Cpe1_{tox}$) in
141 *E. coli* cells resulted in growth inhibition, yielding insufficient amounts of purified protein for
142 structural analyses (**Figure 2a**). Time-lapse microscopy revealed that this growth inhibition was
143 accompanied by reduced cell proliferation and continued elongation, consistent with the proposed
144 cytotoxic activity of Cpe1[37] (**Figure 2b** and **Videos 1-2**). To circumvent this limitation, we co-
145 purified $Cpe1_{tox}$ with its cognate immunity protein, Cpi1, which allowed us to obtain well-
146 diffracting crystals (**Supplementary Figure 3a**). Using selenomethionine-substituted protein, we
147 determined the crystal structure of the $Cpe1_{tox}$–Cpi1 complex at a resolution of 1.87 Å (**Figure 2c**
148 and **Supplementary Table 2**).
149 In our crystal structure, Cpe1 features a six-stranded antiparallel β-sheet flanked by five α-
150 helices on either side, forming the typical α/β core that is characteristic of the PLCP family[51]. The
151 catalytic triad—Cys, His, Asp—is clearly evident and aligns with prior functional predictions[33,51]
152 (**Figure 2c**). Despite sharing limited sequence identity with ABC transporter-associated proteases,
153 a structural homology search using the DALI server identified ComA (Z-score = 16.3; RMSD of
154 1.9 Å across 121 aligned Cα atoms) and LahT (Z-score = 15.9; RMSD of 1.8 Å across 117 aligned
155 Cα atoms) as the closest homologs[50,52,53] (**Figure 2d**). A structural comparison revealed a high
156 conservation of the spatial arrangement of the catalytic triad of Cpe1. Overlaying the Cα atom of
157 the Cpe1 and LahT catalytic residues yielded minor RMSD values (Cys: 0.583Å; His: 0.843Å;
158 Asp: 0.711Å), whereas the catalytic triad of ComA presented a slight shift relative to Cpe1 (RMSD:

159 Cys: 2.444Å, His: 1.812Å, Asp: 1.680Å) with a 39.4° rotation of the cysteine residue (**Figure 2d**).
160 These differences may reflect variations in substrate specificity or catalytic efficiency. Overall, the
161 resolved Cpe1 structure is consistent with its predicted protease function, indicating that its
162 proteolytic activity relies on the common catalytic thiol mechanism (**Figure 1a**).

163 In line with our structural data, mutational analyses revealed that the substitution of the
164 catalytic cysteine with alanine ($Cpe1_{tox}^{C362A}$) abolished Cpe1-mediated toxicity (**Figure 2a**).
165 Moreover, the catalytically inactive Cpe1 mutant failed to induce the cell elongation phenotype
166 observed for wild-type Cpe1, further demonstrating that Cpe1 toxicity is linked to its PLCP activity
167 (**Figure 2b** and **Video 3**). To assess if the catalytic activity of Cpe1 is important for interbacterial
168 antagonism, we performed a growth competition assay using an *E. coli* strain (ATCC-11775)
169 harboring the wild-type Cpe1 toxin and an active T6SS as the donor strain, competing against a
170 recipient *E. coli* model strain (MG1655). Notably, recipient cells exhibited a significant fitness
171 defect when co-cultured with donor cells expressing wild-type Cpe1 (**Figure 2e**). However, this
172 competitive advantage was markedly reduced when donor cells expressed the inactive Cpe1
173 ($Cpe1_{tox}^{C362A}$). These findings demonstrate that the catalytic activity of Cpe1 plays a crucial role
174 in mediating interbacterial competition.

175 Interestingly, although Cpi1 binds to Cpe1 and they share a large interface (1050 $Å^2$), our
176 crystal structure reveals that Cpi1 does not sterically occlude the active site of Cpe1. Instead, Cpi1
177 primarily interacts with a shallow hydrophobic concave region on the surface of Cpe1 that is
178 located adjacent to the catalytic pocket (**Figures 2c, f**). This binding region consists of a cluster of
179 non-polar residues—L387, M390, A408, M426, W428, and V434—the hydrophobic properties of
180 which are conserved across many T6SS– and CDI–associated Cpe1 toxins (**Supplementary**
181 **Figure 1a**). We did not identify any enzymatic domain in or significant structural homologs of

182 Cpi1, suggesting that its neutralization mechanism depends on binding to the hydrophobic concave
183 region of Cpe1 rather than occlusion of its active site.

184 To examine the importance of the Cpe1–Cpi1 interaction, we assessed the ability of Cpi1
185 variants displaying impaired Cpe1 binding to protect against toxicity. By scanning the Cpe1–Cpi1
186 interface, we identified four candidate residues (I47, M61, M64, and K72) in Cpi1, where
187 substitutions were predicted to disrupt the Cpe1–Cpi1 interaction (**Figures 2g**). Single-residue
188 substitutions did not significantly affect the ability of Cpi1 to inhibit Cpe1 toxicity, as these
189 variants retained their immunity function and still bound Cpe1 in co-immunoprecipitation assays
190 (**Figures 2h, i**). However, when we mutated all four residues ($Cpi1^{mut4}$), the resulting mutant
191 lacked the ability to neutralize Cpe1 toxicity and failed to bind Cpe1 *in vitro*, despite being
192 expressed at levels comparable to that of wild-type protein (**Figures 2h, i**, and **Supplementary**
193 **Figure 3b**). In addition, the Cpi1 quadruple mutant did not provide full protection during
194 interbacterial competition (**Figure 2e**). These findings indicate that the interaction between Cpe1
195 and Cpi1 is critical for the immunity function of Cpi1 and that disruption of this interaction
196 abrogates its protective effect (**Figures 2a, b**, and **Video 4**).

197

198 **The Hydrophobic Concave Surface Is Critical for Cpe1 Toxicity**

199 Our structural analysis revealed that Cpe1 shares significant similarities with the cysteine
200 protease domains of ComA and LahT[50,52] (**Figure 2d**). Previous biochemical and structural studies
201 of these proteases have shown that, similar to Cpe1, they also possess hydrophobic concave
202 surfaces adjacent to their catalytic pockets, which are critical for specific recognition of protein
203 substrates[50,52] (**Supplementary Figure 4**). Previous studies have also shown that blocking these
204 hydrophobic regions with high-affinity inhibitors leads to protease dysfunction and impaired

205 substrate transport[50,54]. Given that Cpi1 neutralizes Cpe1 toxicity by interacting with its
206 hydrophobic concave region (**Figure 2f**), we hypothesized that Cpe1 might employ a substrate
207 recognition mechanism analogous to that of ComA and LahT. To test this hypothesis, we
208 introduced mutations into hydrophobic residues within the concave region of Cpe1 (*i.e.,* L387,
209 M426, W428) and assessed their impact on toxicity (**Figure 2f**). Supporting our hypothesis,
210 ectopic expression of the Cpe1 variants in model *E. coli* resulted in a marked reduction in toxicity
211 compared to wild-type Cpe1, without affecting protein expression levels (**Figure 3a**). These
212 findings support the notion that the hydrophobic concave region is important for the cytotoxic
213 activity of Cpe1 and may also contribute to substrate recognition.

214 To further investigate if the hydrophobic concave region of Cpe1 is involved in substrate
215 binding, we carried out site-specific photo-crosslinking experiments, focusing on the residues for
216 which mutations abolished Cpe1-mediated toxicity (**Figure 3a**). We incorporated the photo-
217 reactive amino acid p-benzoyl-L-phenylalanine (Bpa) in place of the selected amino acids using
218 enhanced nonsense suppression[55] (**Figure 3b**). This crosslinking approach provides several
219 advantages, including the ability to introduce the Bpa crosslinker at a single site within Cpe1, and
220 its modestly larger size relative to phenylalanine increases the likelihood of capturing direct
221 interactions with substrates[56]. To prevent Cpe1 from cleaving its bound substrates, we introduced
222 the catalytically inactive C362A mutation into the Cpe1-Bpa variants for our crosslinking
223 experiments.

224 Cells expressing these Cpe1-Bpa variants were directly exposed to long-wavelength UV
225 irradiation (365 nm) to induce covalent crosslinking between Cpe1 and potential substrates
226 (**Figure 3b**). Following UV exposure, Cpe1-Bpa and its crosslinked products were purified using
227 the hexa-histidine tag located at the C-terminus of Cpe1 and analyzed by electrophoresis and

228 immunoblotting. As expected, we observed multiple crosslinked products migrating more slowly
229 by SDS-PAGE than Cpe1-Bpa monomers (*i.e.,* L387Bpa, M426Bpa, W428Bpa) (**Figure 3c**). The
230 molecular weights of the crosslinked products ranged from 30 kDa to 180 kDa, indicating
231 formation of Cpe1-substrate complexes. In contrast, our control samples, which did not incorporate
232 Bpa, presented no high-molecular-weight crosslinked adducts on the gels. Additionally, levels of
233 the Cpe1-Bpa monomers (L387Bpa, M426Bpa, W428Bpa) slightly decreased after UV irradiation,
234 further supporting that Cpe1-Bpa bound and crosslinked to its substrates via the hydrophobic
235 concave region. This decrease in level upon UV irradiation was not observed for a parallel control
236 experiment, indicating that the crosslinking was specific to the modified Cpe1-Bpa variants
237 (**Figure 3c**).
238
239 **Cpe1 Targets the Essential Type II DNA Topoisomerases GyrB and ParE**
240 To define potential protein substrates of the Cpe1 toxin, we subjected purified Cpe1-Bpa
241 crosslinked adducts to mass spectrometric analysis. To minimize false-positive results that could
242 obscure our identification of physiological targets, we applied a stringent cutoff, focusing on
243 proteins with >10 unique peptides, an intensity index >5, and consistent detection across three
244 replicates. Given that many interbacterial toxins associated with the T6SS and CDI pathways are
245 known to target essential cellular components to inhibit or kill competing cells[48], we focused our
246 analysis on essential proteins, though we are aware that non-essential proteins might also
247 contribute to critical cellular processes.
248 Our mass spectrometry analysis revealed 51 cytosolic proteins that were consistently
249 detected across all three Cpe1-Bpa crosslinking experiments (**Supplementary Table 3**). Among
250 these, eight were identified as essential for *E. coli* viability, each playing a critical role in diverse

251 cellular processes[57,58]. These proteins included the type II DNA topoisomerases GyrB and ParE,
252 essential for DNA replication and chromosome segregation; NusA, NusG, and RpoB, involved in
253 transcription; FtsZ, critical for cell division; and AccA and DapE, vital for metabolism (**Figure**
254 **3d**).

255 To validate the substrates of Cpe1, we performed an *in vitro* protease cleavage assay by
256 incubating purified candidate target proteins with $Cpe1_{tox}$. In this assay, $Cpe1_{tox}$ is expected to
257 recognize and cleave the targets, with proteolytic cleavage being confirmed by SDS-PAGE
258 analysis, whereby a reduction in molecular weight and the presence of cleavage fragments
259 indicated substrate digestion. As a result, we observed that two out of the eight essential proteins—
260 type II DNA topoisomerases GyrB and ParE—displayed clear molecular weight reductions upon
261 being incubated with $Cpe1_{tox}$ but not with the catalytically inactive $Cpe1_{tox}^{C362A}$ (**Figures 3e, f** and
262 **Supplementary Figures 5a-f**). Moreover, adding the immunity protein Cpi1 to the reaction
263 inhibited the proteolytic activity of Cpe1 (**Supplementary Figures 5g, h**). Notably, incubating
264 either GyrB or ParE with wild-type $Cpe1_{tox}$ resulted in relatively short but consistent fragments
265 (~12 to 14 kDa), indicating that the cleavage events are specific and may occur toward the termini
266 of these proteins. Collectively, these findings support a model in which Cpe1 targets the essential
267 proteins GyrB and ParE, potentially impairing vital cellular functions as part of a competitive
268 inhibition strategy.

269

270 **Cpe1 Cleaves a Consensus Sequence Containing Double Glycine Motifs within GyrB and**
271 **ParE**

272 Many proteases in the PLCP family cleave peptide bonds at sequence-specific sites[51].
273 Notably, homologs of Cpe1, such as ComA and LahT, recognize and cleave their native substrates

274 at sequences containing a double glycine (GG) motif[50,59,60] (**Supplementary Figures 6a, b**).
275 Accordingly, we hypothesized that Cpe1 might also target its substrates, GyrB and ParE, at a
276 consensus sequence containing two consecutive glycine residues. Protein sequence alignment of
277 GyrB and ParE revealed four consensus sequences containing GG motifs (**Figure 3g**). Two of
278 these motifs, located near the N-terminal ATPase domain: $G_{101}G_{102}$ and $G_{113}G_{114}$ in GyrB, and
279 $G_{97}G_{98}$ and $G_{109}G_{110}$ in ParE, were prioritized for further investigation, as cleavage at these sites
280 would generate ~12 to 14 kDa fragments, *i.e.,* matching those observed in our *in vitro* cleavage
281 assays (**Figures 3e, f**).

282 To confirm these cleavage sites, we purified variants of GyrB and ParE in which one
283 glycine residue had been deleted from each GG motif, and then subjected them to $Cpe1_{tox}$ cleavage
284 assays. Our results showed that removing one of the $G_{101}G_{102}$ residues in GyrB or from $G_{97}G_{98}$ in
285 ParE significantly reduced $Cpe1_{tox}$-mediated cleavage (**Figures 3h, i**). In contrast, mutations in the
286 other GG motifs had no effect on cleavage by $Cpe1_{tox}$. To further characterize the cleavage sites of
287 Cpe1 on its substrates, we analyzed Cpe1-cleaved GyrB and ParE fragments through in-gel
288 digestion followed by mass spectrometry (**Supplementary Figures 6c, d**). LC-MS/MS analysis
289 demonstrated that both GyrB and ParE were cleaved precisely between the glycine residues in the
290 GG motifs located within their ATPase domains (**Supplementary Figures 6e, f**). Together, these
291 findings support the notion that Cpe1 selectively targets consensus sequences containing the
292 $G_{101}G_{102}$ motif in GyrB and the $G_{97}G_{98}$ motif in ParE, reinforcing the substrate specificity of Cpe1
293 (**Figure 3g**).

294

295 **Cpe1-mediated Proteolysis Disrupts DNA Topology and Inhibits Chromosome Segregation**
296 **in Bacteria**

297 GyrB and ParE are members of the type II DNA topoisomerases, forming the hetero-
298 tetrameric DNA gyrase ($GyrB^2/GyrA^2$) and topoisomerase IV ($ParE^2/ParC^2$) complexes,
299 respectively, in bacteria[61]. These enzymes are well characterized for their roles in catalyzing the
300 relaxation of supercoiled DNA in an ATP-dependent manner, thereby facilitating critical biological
301 processes that require modification of DNA topology[62]. Malfunction of DNA gyrase impairs DNA
302 replication, transcription, and repair, whereas inhibition of topoisomerase IV results in abnormal
303 catenation of daughter chromosomes following replication, ultimately blocking cell division[63].
304 These essential activities make both proteins appealing targets for antimicrobial agents in clinical
305 settings[64,65]. Notably, the consensus sequence recognized by Cpe1 is located within a loop
306 connecting helix 3 and helix 4 in the ATPase domain of GyrB and ParE[66,67] (**Figures 4a, b**). This
307 loop is highly conserved across different bacterial species[68] (**Figures 4c, d**), and has been
308 previously identified as a critical region involved in ATP-binding, dimerization, and
309 conformational changes triggered by ATP hydrolysis[67,69,70]. Therefore, cleavage of the loops in
310 GyrB and ParE by Cpe1 would paralyze topoisomerase function, conferring a competitive fitness
311 advantage to antagonistic bacteria by inhibiting DNA replication and chromosome segregation in
312 their rivals.

313 If GyrB and ParE are indeed substrates of Cpe1, we reasoned that Cpe1 intoxication would
314 impair the ability of both enzymes to maintain DNA topology, specifically by decreasing negative
315 supercoiling of cellular DNA. Therefore, we used a high-copy plasmid, pET, isolated from *E. coli*
316 ectopically expressing Cpe1 to visualize changes in DNA topology via high-resolution agarose gel
317 electrophoresis with chloroquine, allowing the resolution of negatively supercoiled DNA. As
318 predicted, plasmid DNA topoisomers extracted from Cpe1-intoxicated cells (0.5 and 1 hour of
319 induction) displayed a significant decrease in negatively supercoiled DNA bands[71] (**Figure 4e**). In

320 contrast, plasmid DNA from cells expressing the catalytic mutant Cpe1^{C362A} showed a high level
321 of plasmid DNA in a relaxed state, *i.e.,* similar to the vector control. This observation mirrors the
322 effects reported previously when the ATPase domains of GyrB or ParE were inhibited or mutated,
323 supporting that the observed changes were attributable to disruption of type II DNA topoisomerase
324 activity[69,72,73].

325 Inactivation of topoisomerase IV is known to result in DNA knotting and catenation,
326 leading to an accumulation of unsegregated DNA at the center of bacterial cells[74]. Fluorescence
327 microscopy validated this notion, revealing unsegregated and condensed DNA in elongated
328 bacteria subjected to Cpe1 intoxication (**Figure 4f** and **Supplementary Figure 7**), representing a
329 phenotype reminiscent of cells treated with novobiocin, an antibiotic that inhibits the ATPase
330 activities of both GyrB and ParE[75,76]. In contrast, sister nucleoids formed and segregated normally
331 in dividing cells expressing either the Cpe1^{C362A} variant or those co-expressing Cpe1 and its
332 cognate immunity protein, Cpi1 (**Figure 4f** and **Supplementary Figure 7**). Given that
333 chromosome partitioning is critical for successful cell division, next we examined if Cpe1
334 intoxication also disrupts the bacterial cell division machinery. To test this possibility, we
335 conducted Cpe1 intoxication experiments on *E. coli* expressing fluorescently labeled cell division
336 protein FtsZ (*i.e.,* FtsZ-mNeonGreen)[77]. As expected, the Z-ring structure that is essential for cell
337 division failed to form at the septa of Cpe1-intoxicated bacteria (**Supplemental Figures 8a, b**).
338 These findings collectively support a model in which Cpe1 targets and cleaves the consensus loops
339 in ATPase domains of GyrB and ParE, disrupting their topoisomerase activity and thereby
340 inhibiting DNA replication, chromosome segregation, and cell division, ultimately resulting in the
341 cessation of bacterial growth (**Figure 4g**).
342

343 **Cpi1 Confers Competitive Inhibition against Cpe1**

344 Our identification of GyrB and ParE as substrates of Cpe1 prompted us to investigate the
345 mechanism by which Cpi1 inhibits Cpe1. Based on the $Cpe1_{tox}$–Cpi1 complex structure, toxicity
346 assays, and site-specific crosslinking experiments, we suspected that Cpi1 binds competitively at
347 the hydrophobic concave region of Cpe1, overlapping with the binding regions of GyrB and ParE,
348 thereby neutralizing Cpe1-mediated intoxication. This competitive inhibition model was supported
349 by AlphaFold3 (AF3) predictions, which revealed that the binding regions for GyrB and ParE on
350 Cpe1 partially overlap with those of Cpi1 in the predicted structures[78] (**Figure 5a**, and
351 **Supplementary Figures 9a, b**). Notably, the loop sequence containing the Cpe1 cleavage site on
352 GyrB actually extends into the catalytic pocket of Cpe1 in the AF3 model structure, supporting our
353 prior characterization of its protease activity and substrate specificity (**Supplementary Figure 9c**).

354 To test the competitive inhibition model, we began by conducting *in vitro* competitive
355 binding assays to determine if Cpi1 could displace substrate interactions with Cpe1 (**Figure 5b**).
356 In our assay, catalytically inactive $Cpe1^{C362A}$ was incubated with the substrate (*e.g.,* the ATPase
357 domain of ParE), which was tagged with a C-terminal strep tag to allow complex formation. The
358 Cpe1/ParE complex was then immobilized on streptavidin resin. The ATPase domain of ParE
359 served as a representative substrate due to its ease of purification and susceptibility to cleavage by
360 wild-type Cpe1, similar to full-length ParE (**Supplementary Figure 9d**). Following complex
361 formation, increasing concentrations of wild-type Cpi1 were added, followed by washing to
362 remove unbound $Cpe1^{C362A}$. As a result, $Cpe1^{C362A}$ levels bound to $ParE_{ATPase}$ were markedly
363 reduced in the presence of Cpi1 in a concentration-dependent manner, indicating that Cpi1
364 displaced $ParE_{ATPase}$ from its interaction with $Cpe1^{C362A}$ (**Figure 5c**). In contrast, in a control
365 experiment using $Cpi1^{mut4}$, in which the Cpe1-binding residues had been mutated (**Figure 2j**), no

366 significant changes in Cpe1^{C362A} level were observed (**Figure 5d**). These findings support that
367 Cpi1 competitively interacts with the substrate-binding site on Cpe1. Based on the observed
368 competition, we reasoned that Cpi1 should exhibit a higher binding affinity to Cpe1 than its target
369 substrates. Using biolayer interferometry, we confirmed that Cpi1 binds to Cpe1^{C362A} with an
370 approximately 40-fold higher affinity than ParE$_{ATPase}$ *in vitro* (K_d: Cpe1^{C362A} –Cpi1 = 8.58 nM;
371 Cpe1^{C362A}–ParE$_{ATPase}$ = 343 nM). However, binding affinity was too low to be measured when
372 Cpi1^{mut4} was used (**Figures 5e, f** and **Supplementary Figure 9e**). Collectively, these results
373 support a model whereby Cpi1 neutralizes Cpe1-mediated intoxication by employing a
374 competitive inhibition mechanism.
375

376 ## Discussion

377 Our study characterizes a widely distributed class of antibacterial effectors displaying
378 papain-like cysteine protease activity, referred to herein as Cpe1, which is found in diverse Gram-
379 negative bacteria. By targeting essential cellular processes in bacteria, these Cpe1 effectors play a
380 critical role in bacterial competition, broadening the known repertoire of bacterial toxins involved
381 in interbacterial antagonism. We have demonstrated that Cpe1 exerts its toxic effect by cleaving
382 key protein substrates, specifically the type II DNA topoisomerases GyrB and ParE, which are
383 indispensable for DNA replication and chromosome segregation. Cpe1 mediates this cleavage by
384 targeting consensus sequences containing GG motifs within the ATPase domains of these proteins,
385 thereby inactivating the topoisomerase function and halting the DNA replication machinery and
386 cell growth. This mechanism provides a competitive advantage to Cpe1-producing strains.

387 Our phylogenetic analysis reveals a complex evolutionary trajectory for Cpe1 homologs,
388 underscoring their occurrence across diverse bacterial phyla and their functional association with

389 secretion systems such as the T6SS and CDI pathways (**Figure 1d**). The broad distribution of Cpe1
390 homologs indicates that horizontal gene transfer has facilitated adaptation of these protease
391 effectors to diverse ecological niches, enabling bacteria to assert competitive dominance in various
392 environments. Furthermore, the lack of correlation between phylogeny and pathway association
393 among Cpe1 homologs supports that selective pressures favor the adoption of Cpe1-like effectors
394 across multiple bacterial lineages, thereby enhancing bacterial fitness in different ecological
395 contexts.

396 Papain-like cysteine proteases are versatile enzymes that cleave peptide bonds in protein
397 targets and are frequently employed as toxic effectors by bacterial pathogens. For example, the
398 bacterial effector OspD3, secreted by *Shigella flexneri*, cleaves host kinases RIPK1 and RIPK3 to
399 evade necroptosis-mediated immune responses during infection[39]. Similarly, the YopT effector
400 from *Yersinia sp.* cleaves Rho-family GTPases, such as RhoA, leading to disruption of the actin
401 cytoskeleton[79]. Additionally, AvrPphB from *Pseudomonas syringae*, induces plant cell death by
402 cleaving the PBS1 kinase through its cysteine protease activity[80,81]. Our findings provide
403 compelling evidence of bacteria leveraging a PLCP-mediated mechanism to intoxicate competing
404 bacteria, as demonstrated by Cpe1 cleavage of essential DNA topoisomerases. Given that
405 interbacterial interactions predate the evolution of eukaryotic cells, it is plausible that PLCP toxins
406 targeting eukaryotic hosts evolved from ancestral PLCPs possessing antibacterial activity.

407 We identified several cellular proteins crosslinked to Cpe1-Bpa from our crosslinking mass
408 spectrometry experiments (**Figures 3b-d**). In addition to GyrB and ParE, six other essential
409 proteins were detected, namely NusA, NusG, RpoB, FtsZ, AccA, and DapE. However, Cpe1
410 exhibited cleavage activity toward GyrB and ParE in our *in vitro* protease cleavage assays, but
411 not against these other six targets (**Figures 3e, f** and **Supplementary Figures 5a-f)**. These false-

412 positive identifications might be due to non-specific interactions with heterologous Cpe1-Bpa
413 expression. Our further analysis of the cleavage sites revealed that Cpe1 recognizes a consensus
414 sequence, LHAGGKF, within a loop region of its substrates and cleaves the peptide bond
415 immediately following the double glycine residues. Deletion of these glycine residues in GyrB and
416 ParE significantly reduced Cpe1 activity *in vitro* (**Figures 3h, i**). The contribution of other amino
417 acid residues within the consensus sequence to Cpe1 activity remains unclear, as does the influence
418 of substrate three-dimensional structure on Cpe1 specificity and cleavage. Systematic analysis of
419 cleavage sequences and structural determinants is required to determine if Cpe1 can recognize and
420 cleave additional substrates in bacteria.

421 In addition to elucidating the role of Cpe1 during interbacterial antagonism, our study
422 identifies a unique immunity mechanism that safeguards Cpe1-producing bacteria from self-
423 toxicity. The cognate immunity protein, Cpi1, binds to a conserved hydrophobic concave surface
424 adjacent to the catalytic pocket of Cpe1 (**Figure 2f**). This interaction prevents Cpe1 from accessing
425 its substrates without occluding the active site of the effector. The coevolutionary relationship
426 between Cpe1 and Cpi1 is evidenced by sequence conservation and structural complementarity.
427 The evolutionary advantage of this mode of inhibition likely lies in the enhanced binding affinity
428 afforded by the large surface area of hydrophobic interaction. Similar mechanisms have been
429 reported for other protease-inhibitor systems. For example, the anticoagulation factor triabin
430 inhibits thrombin protease by binding to regions outside of the catalytic pocket[82,83], and calpastatin
431 neutralizes calpain protease through an exosite interaction, tripling the binding surface compared
432 to other inhibitors[84,85]. Likewise, the anti-toxins of colicin, such as E3 rRNase and E9 DNase, are
433 known to neutralize these toxins by binding with high affinity to the exosites, effectively blocking
434 activity without overlapping the active site[86].

435 Bacterial toxins possessing protease activity have long been proven valuable tools in
436 investigating host cell biology due to their ability to manipulate with precision specific cellular
437 functions. For example, the identification of the protein targeted by the specific endopeptidase
438 activity of the tetanus and botulinum toxins provided fundamental insights into the role of SNARE
439 complex proteins in regulating exocytosis[87,88]. Our finding that Cpe1 specifically cleaves GyrB
440 and ParE has unveiled the possibility of applying this toxin to study DNA replication, catenation,
441 and chromosome segregation, among other aspects of cell biology. Although the general functions
442 of these topoisomerases are already well established, certain mechanistic aspects remain unclear[89].
443 Given its precise targeting of the ATPase domains of GyrB and ParE, Cpe1 could serve as a
444 valuable tool for dissecting the finer details of certain critical processes.
445 In conclusion, our study provides a detailed characterization of Cpe1 as a potent
446 interbacterial toxin that targets essential DNA topoisomerases in competitor cells. By broadening
447 the functional scope of PLCPs in bacterial competition and elucidating the molecular mechanisms
448 underlying immunity against Cpe1, our findings lay the groundwork for further exploration of how
449 PLCPs function within microbial communities. The substrate specificity and potent activity of
450 Cpe1 highlight its potential for applications in developing analogs or inhibitors that replicate its
451 targeting mechanism. Furthermore, insights into the Cpi1 immunity mechanism could inform the
452 engineering of bacterial strains presenting enhanced resistance to PLCP-mediated antagonism,
453 opening up avenues for biotechnological applications such as microbiome manipulation and the
454 creation of next-generation antibacterial therapies.
455
456
457

458 # Methods

459 **Bioinformatic Analysis of Cpe1 and Cpi1-related Proteins**

460 The protein sequences of the full-length PLCP effectors EvpQ (GenBank:
461 JACQ01000015.1, 119,565-120,092 basepairs) and TsaP (accession number: AJM72455.1) were
462 obtained from the NCBI database, as described in previous studies[36,37]. The cysteine protease
463 domains within these sequences were identified using the NCBI Conserved Domain Search tool[90]
464 and subsequently used as seed sequences for PSI-BLAST[45]. PSI-BLAST was run iteratively until
465 convergence, with a relatively lenient e-value cut-off of 0.01 to ensure inclusion of highly
466 divergent homologs. To minimize false-positive hits, the retrieved sequences were filtered to retain
467 only those with a minimum length of 100 amino acids.

468 Interbacterial PLCP effectors were manually curated based on their genomic context within
469 gene clusters associated with contact-dependent antagonistic pathways (*i.e.,* T6SS, CDI)[91,92].
470 Effector-associated domains known to mediate interbacterial antagonism, such as PAAR, VgrG,
471 and Rhs for T6SS, or VENN and filamentous hemagglutinin peptide repeats for CDI, were used
472 to validate their functional relevance[46,47]. Taxonomic and strain-level information for the identified
473 PLCP effectors was retrieved from NCBI. Multiple sequence alignments of the homologs were
474 performed using ClustalW[93], and a maximum likelihood phylogenetic tree was constructed using
475 the IQtree online tool with default parameters[94]. The resulting tree was visualized and edited using
476 Figtree (http://tree.bio.ed.ac.uk/software/figtree/).

477

478 **Bacteria and Culture Conditions**

479 The bacterial strains used in this study are listed in **Supplementary Table 4**. The following
480 *Escherichia coli* strains were used: DH5α and PIR1 for cloning and plasmid maintenance; S17-1

481 λ pir for conjugal transfer of the pRE118 plasmid into *E. coli*; and BL21 (DE3) for overproduction
482 and purification of protein samples. *E. coli* ATCC-11775 and MG1655 were used for toxicity assay
483 and bacterial competition assays. Bacterial strains were routinely grown in Luria Bertani (LB)
484 medium supplemented with appropriate antibiotics at 37°C with shaking at 200 rpm. Antibiotics
485 and chemicals were used at the following concentrations: 50 μg/mL for kanamycin, 25 μg/mL for
486 chloramphenicol, 150 μg/mL for carbenicillin, 0.25 mM isopropyl β-D-1-thiogalactopyranoside
487 (IPTG), 0.2% (*w/v*) L-(+)-arabinose, and 10% (*w/v*) sucrose.
488
489 **Plasmid Construction**
490 All plasmids and primers used in this study are listed in **Supplementary Table 4**.
491 Mutations in *E. coli* were generated using the pRE118 vector[95]. For chromosomal mutation
492 constructs, 800-basepair regions flanking the mutation site were amplified by polymerase chain
493 reaction (PCR), sewn together, and inserted into the vector using Gibson assembly at the *XbaI* and
494 *SacI* restriction sites[96]. Insertions at the Tn7 sites of *E. coli* strains were generated using the
495 pUC18mini R6K vector with the target genes amplified by PCR and inserted into the vector
496 through Gibson assembly at the *XhoI* and *SacI* restriction sites[97].
497 For co-expression and purification of the $Cpe1_{tox}$–Cpi1 complex, the $cpe1_{tox}$ and *cpi1* genes
498 were amplified and cloned into MCS (multiple cloning site)-1 (*BamH1* and *NotI* sites) and MCS-
499 2 (*NdeI* and *XhoI* sites) of the pETDuet-1 vector, respectively, resulting in N-terminal hexa-
500 histidine fusion to $cpe1_{tox}$. Candidate protein substrates of $Cpe1_{tox}$ were purified by cloning the
501 corresponding genes into MCS-1 of pETDuet-1. The *BamHI* and *NotI* sites were used to N-
502 terminally fuse hexa-histidine to substrates (*e.g.,* GyrB and ParE)[98]. Alternatively, the *NcoI* and
503 *NotI* sites were employed for C-terminal hexa-histidine fusions to substrates (*e.g.,* NusA, NusG,

504 RpoB, AccA, and DapE) or for expressing proteins without fusion tags (*e.g.,* FtsZ). For strep-
505 tagged proteins (*e.g.,* Cpi1 variants and the ATPase domain of ParE) and His-tagged Cpi1, the
506 corresponding genes were cloned into MCS-2 of pETDuet-1 using the *NdeI* and *XhoI* restriction
507 sites.

508 Site-directed mutagenesis was performed to generate substitution mutants of toxin and
509 immunity proteins in pBAD33 and pETDuet-1 plasmids. Primers containing the desired mutations
510 were paired with a complementary primer in the opposite orientation to amplify a mutated copy of
511 the plasmid. The template plasmid was digested using *DpnI*, and the resulting mutated amplicon
512 was transformed into *E. coli* competent cells. Mutant plasmids were selected by growth on plates
513 containing carbenicillin (for pETDuet-1) or chloramphenicol (for pBAD33).

514

515 **Generation of Mutant Strains of *E. coli***

516 To generate mutations of *E. coli* ATCC-11775 strains, mutant constructs in pRE118
517 plasmid were transformed into *E. coli* S17-1 λ pir. *E. coli* S17-1 λ pir donor strains carrying the
518 mutant constructs and *E. coli* ATCC-11775 recipient strains to be mutated were grown overnight
519 on LB plates containing appropriate antibiotics, then scraped together to create a 1:1 mixture of
520 each donor-recipient pair that was spread on an LB agar plate and incubated at 37°C for 6 hours
521 to facilitate plasmid transfer via conjugation. Cell mixtures were then scraped into LB and plated
522 on LB agar containing kanamycin and chloramphenicol to select for *E. coli* ATCC-11775 with
523 integrated plasmid. *E. coli* ATCC-11775 merodiploid strains were then grown overnight in a non-
524 selective LB medium at 37°C, followed by counter-selection by plating on nutrient agar plates
525 supplemented with sucrose. Kanamycin-sensitive, sucrose-resistant colonies were screened for

526 allelic replacement by colony PCR, and mutations were confirmed by Sanger sequencing of the
527 PCR products.

528 To generate *E. coli* MG1655 strains with insertions at the Tn7 site, pUC18mini_R6K
529 plasmids carrying the insert fragments and the helper plasmid pTNS3 were co-transformed into *E.*
530 *coli* MG1655 through electroporation[97]. Following electroporation, the cell suspension was
531 incubated in SOB media at 37°C for 1 hour for recovery. The cells were then plated onto LB agar
532 containing kanamycin for selection. Kanamycin-resistant colonies were screened for the presence
533 of insertions using colony PCR, and mutations were confirmed by Sanger sequencing of the PCR
534 products.

535

536 **Cpe1 Toxicity Assays**

537 To assess the toxicity of $Cpe1_{tox}$ variants and the protective effect conferred by expression
538 of Cpi1 variants, overnight cultures of *E. coli* BL21 (DE3) harboring toxin and immunity genes in
539 pBAD33 and pETDuet-1 vectors, respectively, were used to inoculate LB medium. Cultures were
540 adjusted to an initial optical density (OD_{600}) of 0.05 and incubated at 37°C with shaking at 200
541 rpm for 4 hours in the presence of appropriate inducers. Following incubation, 10-fold serial
542 dilutions of each culture were prepared and plated onto LB agar to determine colony-forming units
543 (CFUs). Unless otherwise specified, $Cpe1_{tox}$ expression was induced by the addition of arabinose
544 to cultures harboring pBAD33, whereas expression of Cpi1 from pETDuet-1 was induced by the
545 addition of IPTG.

546

547

548

549 **Bacterial Competition Assays**

550 For each competition experiment, *E. coli* ATCC-11775 Δ*hns* was used as the donor strain,
551 whereas *E. coli* MG1655 served as the recipient strain. The Δ*hns* mutation was introduced into the
552 donor strain to upregulate T6SS activity as previously described[99-101]. The indicated *E. coli* donor
553 and recipient strains were cultured for 16 hours in LB broth at 37°C. The overnight cultures were
554 then refreshed by inoculating LB medium at a ratio of 3:100 (culture:medium) and incubated at
555 37°C for 5 hours. After incubation, cells were harvested by centrifugation at 17,900 × *g* for 1
556 minute. The supernatant was discarded, and the cell pellets were washed once with LB medium.
557 The cells were centrifuged again, resuspended in LB, and normalized to an OD_{600} of 2. Donor and
558 recipient strains were then mixed at a 50:1 (*v/v*) ratio, and the initial donor-to-recipient ratios were
559 determined by performing 10-fold serial dilutions and plating on selective media. Competitions
560 were initiated by spotting 3 × 5 μL of each mixture onto nitrocellulose filters placed on LB agar
561 plates containing 3% (*w/v*) agar. The plates were incubated at 37°C for 6 hours. Following
562 incubation, cells were harvested by scraping individual spots from excised sections of the
563 nitrocellulose filter into LB medium. The suspensions were serially diluted and plated on selective
564 media to quantify CFUs.

565

566 **Analysis of Protein Expression Levels**

567 To analyze the expression of $Cpe1_{tox}$ and Cpi1 variants, *E. coli* strains harboring the
568 plasmids expressing the target proteins were cultured in LB medium supplemented with
569 appropriate inducer at 37°C. Cells were harvested at an OD_{600} of 1, and cell pellets were
570 resuspended in SDS sample buffer for analysis. The samples were boiled at 100°C for 10 minutes,
571 and then subjected to SDS-PAGE. Proteins were transferred onto nitrocellulose membranes, which

572 were then blocked in TBST buffer (10 mM Tris-HCl pH 7.5, 150 mM NaCl, 0.1% (*v/v*) Tween-20)
573 containing 5% (*w/v*) non-fat milk for 30 minutes at room temperature. Blocked membranes were
574 incubated with primary antibodies (α-His, α-Strep, or α-RNA Polymerase β) diluted in TBST for
575 1 hour at room temperature. Following incubation, the membranes were washed with TBST and
576 subsequently incubated for 30 minutes at room temperature with a secondary antibody (α-mouse
577 IgG HRP-conjugated) diluted 1:5000 in TBST. After the wash with TBST, protein detection and
578 visualization were performed using a UVP BioSpectrum 815 system.
579
580 **Protein Purification**
581 To prevent cytotoxicity during overexpression in *E. coli*, all $Cpe1_{tox}$ constructs were co-
582 expressed with Cpi1 from pETDuet-1 in *E. coli* BL21 (DE3). Stationary-phase cultures of the
583 expression strains were used to inoculate 1 liter of LB broth supplemented with carbenicillin,
584 which was then incubated in a shaking (200 rpm) incubator at 37°C until the mid-log phase (OD_{600}
585 = 0.4 - 0.7). Protein expression was induced by adding IPTG, followed by incubation at 30°C for
586 5 hours. Cells were harvested by centrifugation at 7,000 × *g* for 30 minutes and resuspended in
587 lysis buffer (50 mM Tris-HCl pH 7.5, 500 mM NaCl, 5 mM imidazole, 1 mM DTT, 5% (*w/v*)
588 glycerol, and 1 mg/mL lysozyme). Resuspended cells were incubated on ice for 30 minutes,
589 disrupted by sonication (10 pulses of 10 seconds each), and centrifuged at 40,000 × *g* for 30
590 minutes to remove cellular debris. His-tagged $Cpe1_{tox}$ and associated proteins were purified from
591 the supernatant using a 2 mL Ni-NTA agarose column by gravity flow. Bound proteins were eluted
592 using a linear imidazole gradient, reaching a final concentration of 300 mM. Purity was assessed
593 by SDS-PAGE, followed by Coomassie Brilliant Blue staining. For further purification, protein
594 samples were subjected to fast protein liquid chromatography (FPLC) using gel filtration on a

595 HiLoad 16/600 Superdex 200 pg column (GE Healthcare). Fractions demonstrating high purity
596 were collected and used in biochemical assays. For selenomethionine-incorporated $Cpe1_{tox}$–Cpi1
597 complex, cells were grown in SelenoMethionine Medium Complete (Molecular Dimensions)
598 under the same expression conditions described above. Cell lysis, Ni-NTA affinity purification,
599 and gel filtration were performed as detailed for native proteins.

600 To obtain free $Cpe1_{tox}$ for experiments, a denaturation and refolding strategy was employed
601 to separate His-tagged $Cpe1_{tox}$ from Cpi1. The protein mixture was first diluted 1:25 into
602 denaturation buffer (20 mM Tris-HCl pH 7.5, 300 mM NaCl, 1 mM DTT, and 8 M urea) to
603 denature the protein complex. Denatured proteins were then loaded onto a column containing 1
604 mL of Ni-NTA agarose, allowing selective binding of His-tagged $Cpe1_{tox}$ while dissociated Cpi1
605 was removed in the flow-through. On-column refolding was achieved by sequential washing with
606 renaturation buffer (20 mM Tris-HCl pH 7.5, 300 mM NaCl, and 1 mM DTT). The refolded protein
607 was subsequently eluted with elution buffer (20 mM Tris-HCl pH 7.5, 300 mM NaCl, and 300 mM
608 imidazole). Eluted protein samples were dialyzed against storage buffer (20 mM Tris-HCl pH 7.5,
609 300 mM NaCl, 1 mM DTT, and 5% (*w/v*) glycerol) to remove residual imidazole and stabilize the
610 protein. Dialyzed samples were then aliquoted and stored at −80°C for subsequent experiments.

611 To purify Cpe1 candidate protein substrates (GyrB, ParE, NusA, NusG, RpoB, AccA, and
612 DapE) and Cpi1, His-tagged proteins were expressed in *E. coli* BL21 (DE3) transformed with the
613 pETDuet-1 expression vector containing the corresponding coding regions. Cultures were grown
614 in LB broth at 37°C to mid-log phase and induced with IPTG, followed by 2-hour incubation at
615 37°C. Cells were harvested by centrifugation, resuspended in lysis buffer (20 mM Tris-HCl pH 7,
616 300 mM NaCl, 10 mM imidazole, 1 mM DTT, and 1 mg/mL lysozyme), and incubated on ice for
617 30 minutes. The cells were disrupted by sonication (10 pulses, 10 seconds each), and the lysate

618 was cleared by centrifugation at 40,000 × *g* for 30 minutes. His-tagged proteins were purified from
619 the supernatant by means of gravity flow through a 1 mL Ni-NTA agarose column. Proteins bound
620 to the column were eluted with a linear imidazole gradient up to 300 mM. The purity of each
621 protein sample was verified by SDS-PAGE followed by Coomassie Brilliant Blue staining.
622 Purified proteins were resuspended and dialyzed into storage buffer (20 mM Tris-HCl pH 7, 300
623 mM NaCl, 1 mM DTT, and 5% (*w/v*) glycerol). Protein aliquots were frozen and stored at −80°C
624 for further use.

625 For purification of FtsZ, FtsZ was overproduced in *E. coli* BL21 (DE3) transformed with
626 the pETDuet-1 expression vector containing the FtsZ coding region. Cultures were grown in LB
627 medium at 37°C to mid-log phase and induced with IPTG, followed by 3-hour induction at 37°C.
628 The cells were harvested by centrifugation, resuspended in lysis buffer (50 mM Tris-HCl pH 8,
629 100 mM NaCl, 1 mM EDTA, 5 mM $MgCl_2$, 1 mM PMSF, and 0.1 mg/mL lysozyme), and
630 incubated on ice for 30 minutes. Cell lysis was performed by sonication (10 pulses, 10 seconds
631 each), and the lysate was cleared by centrifugation at 40,000 × *g* for 30 minutes. To remove
632 unwanted proteins, the supernatant was subjected to ammonium sulfate fractionation. Proteins
633 precipitated at 20% (*w/v*) ammonium sulfate were discarded, whereas those precipitated at 30%
634 (*w/v*) ammonium sulfate were collected by centrifugation at 40,000 × *g* for 30 minutes. The
635 resulting pellet, enriched for FtsZ, was resuspended in buffer containing 20 mM Tris-HCl pH 8,
636 100 mM NaCl, 1 mM EDTA, and 5 mM $MgCl_2$. The resuspended proteins were dialyzed against
637 storage buffer (20 mM Tris-HCl pH 8, 100 mM NaCl, 0.1 mM EDTA, and 5% (*w/v*) glycerol),
638 aliquoted, and stored in a freezer at −80°C.

639 For purification of proteins with strep tags (*i.e.,* Cpi1 variants and the ATPase domain of
640 ParE), the proteins were overproduced in *E. coli* BL21 (DE3) transformed with the pETDuet-1

641 expression vector containing the respective gene coding regions. Cultures were grown in LB
642 medium at 37°C to mid-log phase and induced by the addition of IPTG. After 2-hour induction at
643 37°C, the cells were harvested by centrifugation and resuspended in lysis buffer (20 mM Tris-HCl
644 pH 7, 300 mM NaCl, 1 mM DTT, and 1 mg/mL lysozyme). The cells were incubated on ice for 30
645 minutes, followed by sonication (10 pulses, 10 seconds each) to achieve lysis. Cellular debris was
646 removed by centrifugation at 40,000 × *g* for 30 minutes. Strep-tagged proteins were purified from
647 the supernatant using a 1 mL gravity-flow column containing streptavidin resin (IBA Lifesciences
648 GmbH). Bound proteins were eluted with a buffer containing 20 mM Tris-HCl pH 7, 300 mM
649 NaCl, 1 mM DTT, and 2.5 mM desthiobiotin. Protein purity was evaluated by SDS-PAGE,
650 followed by Coomassie Brilliant Blue staining. Samples were further purified by means of FPLC
651 on a HiLoad 16/600 Superdex 200 pg column (GE Healthcare).
652
653 **Crystallization and Structure Determination**
654 The $Cpe1_{tox}$–Cpi1 complex was prepared for crystallization by dialyzing the purified
655 protein complex into a buffer containing 5 mM Tris-HCl (pH 7), 150 mM NaCl, and 0.5 mM tris(2-
656 carboxyethyl)phosphine (TCEP). The protein solution was then concentrated to 13.5 mg/mL using
657 spin filtration (10 kDa cutoff, Millipore). Crystallization trials were conducted using commercially
658 available screens from Hampton Research. Diffraction-quality crystals were obtained after two
659 weeks at 20°C using the hanging-drop vapor diffusion method with a protein-to-buffer ratio of 1:2.
660 The crystallization solution consisted of 0.4 M magnesium formate and 0.1 M sodium acetate (pH
661 4.6). Crystals of the selenomethionine-labeled $Cpe1_{tox}$–Cpi1 complex were grown under identical
662 conditions as the native complex, with the protein sample also concentrated to 13.5 mg/mL and

663 mixed at a 1:2 ratio with the same crystallization solution. Crystals were cryoprotected using a
664 solution of 20% (*v/v*) glycerol in the crystallization mother liquor prior to data collection.

665 Native and multiple-wavelength anomalous diffraction (MAD) datasets were collected at
666 beamlines TPS-05A and TLS-BL15A of the National Synchrotron Radiation Research Center
667 (Taiwan). Diffraction data were processed using the HKL2000 software suite[102]. Phase
668 determination was performed using PHENIX with data collected at the selenium peak wavelength
669 from selenomethionine-labeled crystals[103]. The initial model of the $Cpe1_{tox}$–Cpi1 complex was
670 constructed using the electron density map in Coot and subsequently refined using PHENIX[103,104].
671 The crystals belonged to the cubic space group P43212, with two protein complexes per
672 asymmetric unit. No residues were found in the disallowed regions of the Ramachandran plot.
673 Data collection and refinement statistics are provided in **Supplementary Table 2**.

674

675 **Bpa Photo-Crosslinking Experiment**

676 *E. coli* BL21 (DE3) cells were transformed with plasmids encoding $Cpe1_{tox}^{C362A}$
677 containing a TAG stop codon at specific sites (*i.e.,* L387, M426, and W428) to incorporate Bpa
678 via nonsense suppression during translation. The transformation also included the Bpa-tRNA
679 plasmid (pSUPT/BpF), which encodes the tRNA and tRNA synthetase necessary for Bpa
680 incorporation, as described previously[105].

681 The transformed cells were grown in LB medium supplemented with 1.5 mM of Bpa at
682 37°C until reaching the mid-log phase. Protein expression was induced by adding IPTG and
683 arabinose, and the cultures were incubated at 30°C for 3 hours. Cells corresponding to 50 OD_{600}
684 units were harvested, resuspended in 1 mL of ice-cold phosphate-buffered saline (PBS), and
685 divided into two aliquots. One aliquot was exposed to 365 nm UV light (Stratalinker 1800 UV

686 irradiator) for 30 minutes at 4°C to induce crosslinking, while the other aliquot was kept on ice as
687 a non-crosslinked control. Cell lysis was performed by sonication in lysis buffer (20 mM Tris-HCl
688 pH 7.5, 300 mM NaCl, 10 mM imidazole, 8 M urea, and 1 mM DTT). The lysates were incubated
689 with Ni-NTA resin for 2 hours at 4°C to purify His-tagged proteins. Bound proteins, including
690 crosslinked products, were analyzed using immunoblotting and mass spectrometry.
691
692 **Mass Spectrometry**
693 For our interactome analysis, Bpa-crosslinked $Cpe1_{tox}^{C362A}$-protein complexes were
694 purified and immobilized on Ni-NTA resins. After washing four times in lysis buffer, the resins
695 were resuspended in 8 M urea and Tris-HCl pH 8. For cysteine alkylation, 10 mM TCEP and 40
696 mM 2-chloroacetamide (CAA) were added into the samples and incubated at 45°C for 30 minutes
697 with shaking (1500 rpm). The samples were diluted 4-fold with 50 mM Tris-HCl pH 8 and digested
698 by 0.4 µg Lys-C (Wako, Japan) treatment for 3 hours at room temperature and 1 µg of trypsin
699 (Sigma, MO) overnight at 37°C. Supernatants containing digested peptides were acidified by 1%
700 TFA, desalted using the Oasis HLB 1 cc Vac Cartridge (Waters Corp), reconstituted in 80%
701 acetonitrile (ACN), and vacuum-dried at 45°C.
702 NanoLC−nanoESi-MS/MS analysis was performed on a Thermo UltiMate 3000
703 RSLCnano system connected to a Thermo Orbitrap Fusion mass spectrometer (Thermo Fisher
704 Scientific, Bremen, Germany) equipped with a nanospray interface (New Objective, Woburn, MA).
705 Peptide mixtures were loaded onto a 75 µm ID, 25 cm long PepMap C18 column (Thermo Fisher
706 Scientific) packed with 2 µm particles with a pore size of 100 Å and they were separated using a
707 segmented gradient from 5% to 25% solvent B (0.1% formic acid in ACN) in 82.5 minutes and to
708 35% solvent B in 7.5 minutes at a flow rate of 300 nL/minute. Solvent A was 0.1% formic acid in

709 water. The mass spectrometer was operated in the data-dependent mode. In brief, survey scans of
710 peptide precursors from 350 to 1600 m/z were performed at 120K resolution with a 2×10^5 ion
711 count target. Tandem MS was performed by isolation window at 1.6 daltons with the quadrupole,
712 HCD fragmentation with a normalized collision energy of 30, and MS 2 scan analysis at 30K
713 resolution in the orbitrap. The MS 2 ion count target was set to 5×10^4 and the max injection time
714 was 54 milliseconds. Only those precursors with charge states 2–6 were sampled for MS 2. The
715 instrument was run in top speed mode with 3-second cycles. The dynamic exclusion duration was
716 set to 11 seconds with a 10-ppm tolerance around the selected precursor and its isotopes.
717 Monoisotopic precursor selection was turned on. Raw data were processed using MaxQuant
718 software[106,107].

719 To identify digested peptides of Cpe1, the samples were prepared based on a previous study
720 with minor modifications[108]. The protein band from SDS-PAGE was manually excised and cut into
721 small pieces (0.5 mm^3). The excised gel pieces were washed with a solution containing 25 mM
722 NH_4HCO_3 and 40% methanol, followed by 100% ACN. The proteins in gel pieces were treated
723 with 10 mM DTT and then with 55 mM iodoacetamide. Proteins were digested with trypsin
724 (Promega) to a final substrate: trypsin ratio of 50:1 in buffer containing 25 mM ammonium
725 bicarbonate and 10% ACN for 12 to 16 hours at 37°C. The reaction was stopped by adding 5%
726 formic acid.

727 For MALDI-TOF analysis, an aliquot (0.5 μL) of the supernatant from the digest was
728 deposited onto a 384/600-μm MTP AnchorChip (Bruker Daltonik GmbH) target and allowed to
729 air dry at room temperature. Then, an aliquot (0.5 μL) of CHCA solution (1.4 mg/ml α-Cyano-4-
730 hydroxycinnamic acid in buffer containing 0.1% TFA, 1 mM ammonium phosphate, and 85%
731 ACN) was added to the chip and allowed to air dry. Further MALDI-TOF MS mass spectrometry

732 analysis was performed in positive ion mode with delayed extraction (reflection mode) on a Bruker
733 Autoflex maX MALDI-TOF/TOF mass spectrometer (Bremen, Germany) equipped with a 200 Hz
734 SmartBean Laser. Data acquisition and processing were done manually by using FlexControl 3.4
735 and Flex-Analysis 3.4 (Bruker Daltonik GmbH), respectively. The processed data were further
736 analyzed with Biotools 3.2 (Bruker) packaged by assessing the online Mascot server to identify
737 the corresponding polypeptides.

738 For tandem mass spectrometry analysis, peptides were analyzed using an UltiMate™ 3000
739 RSLCnano UHPLC system (Thermo Fisher Scientific) equipped with a capillary C18 column
740 (Waters, nanoEase, 130 Å, 1.7 µm, 75 µm × 250 mm). Separation was achieved with a gradient of
741 3% to 35% buffer B (0.1% formic acid in acetonitrile) in buffer A (0.1% formic acid in water) at a
742 flow rate of 300 nL/min. The system was subsequently washed with 80% buffer B and
743 reconditioned to 3% buffer B. The chromatography system was coupled to a Q-Exactive mass
744 spectrometer (Thermo Fisher Scientific) via a Nanospray Flex Ion source. The mass spectrometer
745 was operated in Full-MS/ddMS2 (Top N) mode, scanning a range of m/z 350–1600 at a resolution
746 of 70,000 FWHM with an AGC target of 3×10^6. MS2 spectra were acquired in HCD mode with
747 a normalized collision energy of 27%, a resolution of 17,500, an injection time of 100 ms, and an
748 AGC target of 1×10^5. The top ten precursors were selected for MS2 analysis using a 2.0 m/z
749 isolation window and a dynamic exclusion time of 20 seconds. Raw LC-MS/MS data were
750 analyzed using Proteome Discoverer 2.5 (Thermo Fisher Scientific). MS/MS spectra were filtered
751 using the Spectrum Selector in Proteome Discoverer with default settings. The spectra were
752 searched against the GyrB and ParE protein sequence databases using the SEQUEST HT and
753 Byonic algorithms. Searches were performed in semi-specific mode to identify peptides resulting
754 from specific cleavage at one terminus. The precursor mass tolerance was set to 10 ppm, and the

755 fragment mass tolerance was 0.02 Da. Trypsin was used as the protease in semi-specific mode.
756 Carbamidomethylation of cysteine was specified as a fixed modification, while N-terminal
757 acetylation and methionine oxidation were included as variable modifications. Peptide spectrum
758 matches (PSMs) were validated using Percolator, with a false discovery rate (FDR) threshold of
759 1%.
760
761 ***In Vitro* Protease Cleavage Assay**
762 Purified protein substrates were incubated with $Cpe1_{tox}$ (wild-type or catalytic mutant) at a
763 10:1 ratio. Reactions were performed at 20°C for 5 minutes in a final volume of 20 µL containing
764 20 mM Tris-HCl pH 7, 300 mM NaCl, and 1 mM DTT. The reactions were stopped by cooling on
765 ice and the addition of an equal volume of SDS sample buffer. Samples were boiled and analyzed
766 by SDS-PAGE, followed by Coomassie Brilliant Blue staining.
767
768 **Plasmid DNA Supercoiling Assay**
769 To visualize variations of DNA topology in bacteria, we followed the procedures described
770 in a previous study with minor modifications[109]. Overnight precultures of strains carrying
771 pBAD33-$Cpe1_{tox}$ (wild-type or catalytic mutant) and the reporter plasmid pET were refreshed in
772 LB broth and incubated at 37°C with shaking (250 rpm). When cultures reached the mid-log phase,
773 cells were transferred to a medium containing arabinose inducer and incubated for an extended
774 period to induce $Cpe1_{tox}$ expression and intoxication. Cells were pelleted by centrifugation, and
775 plasmid DNA was purified using the QIAprep Spin Miniprep Kit (Qiagen) and eluted by 50 mM
776 Tris-HCl pH 8.5. DNA topoisomers were resolved on a 1% (*w/v*) agarose gel containing Tris-
777 acetate-EDTA (TAE) and 5 µg/ml chloroquine. The gels were run in TAE buffer with 5 µg/mL

778 chloroquine for 10 hours (140 volts for 30 minutes, followed by 110 volts for 9.5 hours), stained
779 with 0.5 μg/mL ethidium bromide in TAE buffer, destained in distilled water overnight, and imaged
780 with a Quantum CX5 imaging system (Vilber).
781
782 **Fluorescence and Phase Contrast Microscopy**
783 Imaging was performed using a DeltaVision Core Deconvolution Microscopy system with
784 an Olympus IX71 microscope and a 60x 1.42 NA oil-immersion objective. For fluorescence and
785 phase contrast microscopy, bacterial cultures at the mid-log phase were used to inoculate LB
786 medium supplemented with arabinose and IPTG for the expression of $Cpe1_{tox}$ and Cpi1,
787 respectively. After 3 hours of incubation at 37°C with shaking (200 rpm), cells were harvested by
788 centrifugation at 18,000 × *g* for 1 minute. The culture supernatant was removed and washed with
789 ice-cold PBS. The washed cells were resuspended in PBS containing 70% ethanol for 15-minute
790 cell fixation on ice. The fixed cells were subjected to one PBS wash. Addition of DAPI to the cell
791 suspensions preceded a 5-minute incubation on ice in the dark. The cells were then washed with
792 PBS at 18,000 × *g* for 1 minute. The cell suspensions were then adjusted to OD_{600} = 0.5 using PBS
793 and spotted on a 1.5% (*w/v*) agarose pad settled on a microscope slide.
794 For time-lapse imaging of living cells, single colonies from LB agar were inoculated into
795 LB media supplemented with appropriate antibiotics. After incubation for 16 hours at 37°C with
796 shaking (200 rpm), the cultures were adjusted to OD_{600} = 0.5 before spotting on a 1.5% (*w/v*)
797 agarose pad containing arabinose, IPTG, and appropriate antibiotics settled on a microscope slide.
798 Phase contrast images for each sample were acquired at 10-minute intervals.
799
800

801 **$Cpe1_{tox}$–Cpi1/$ParE_{ATPase}$ Competitive Binding Assay**

802 His-tagged $Cpe1_{tox}^{C362A}$ protein was incubated with an excess of strep-tagged $ParE_{ATPase}$
803 for 1 hour at 4°C, followed by incubation with streptavidin resin (IBA Lifesciences GmbH). After
804 binding, the resin was washed with ice-cold buffer (20 mM Tris-HCl pH 7, 300 mM NaCl, and 1
805 mM DTT) to remove unbound proteins. Increasing concentrations of indicated Cpi1 proteins (His-
806 tagged) were added and incubated at 4°C for 1 hour, followed by a single wash with ice-cold buffer.
807 Bound proteins were eluted with buffer containing 20 mM Tris-HCl pH 7, 300 mM NaCl, 1 mM
808 DTT, and 2.5 mM desthiobiotin. Eluted samples were analyzed by SDS-PAGE, followed by
809 Coomassie Brilliant Blue staining.

810

811 **Biolayer Interferometry (BLI)**

812 BLI was performed using an 8-channel Gator® Plus instrument (Gator Bio) with Data
813 Acquisition V 2.15.5.1221 software (Gator Bio). Experiments were conducted at 30°C with
814 shaking at 1000 rpm. We immobilized 500 nM strep-tagged Cpi1, $Cpi1^{mut4}$, or $ParE_{ATPase}$ onto
815 strep-tactin XT-coated biosensor tips (IBA Lifesciences). Equilibrium binding dose-response
816 curves were generated by varying the concentrations of His-tagged $Cpe1_{tox}^{C362A}$ in BLI buffer
817 (0.2% (*w/v*) BSA, 0.02% (*v/v*) Tween-20 in PBS). For Cpi1 and $Cpi1^{mut4}$, the association and
818 dissociation intervals were conducted 150 and 300 seconds, whereas both intervals were set as 120
819 seconds for $ParE_{ATPase}$. BLI data analysis included reference channel subtraction and Savitzky–
820 Golay filtering. Kinetic parameters were determined using a 1:1 global fitting model with R_{max}
821 values linked across sensors. The interaction between $ParE_{ATPase}$ and His-tagged $Cpe1_{tox}^{C362A}$
822 exhibited fast-on-fast-off kinetics. Therefore, steady-state analysis of the response curves was

823 employed to calculate the Kd and nominal R_{max} values. All data represent results from at least three
824 independent experiments.
825
826 **Generation of Sequence Logos**
827 Protein sequences of 35,812 GyrB homologs and 14,212 ParE homologs were retrieved
828 from the UniProt database[110]. Regions containing the consensus sequence (LHAGGKF) were
829 extracted and aligned using ClustalW[93]. The results were visualized as a sequence logo using the
830 WebLogo3 online tool[111]. Sequences flanking the substrate cleavage sites were obtained from
831 previous studies to generate the sequence logo for the consensus sequences on the substrates of
832 ComA and LahT[50,60]. Sequence conservation was analyzed according to the same ClustalW
833 alignment and visualization procedures.
834
835 **Quantification and Statistical Analysis**
836 Statistical significance in bacterial co-culture and competition assays was assessed by
837 unpaired two-tailed t-tests between relevant samples. Values for statistical significance are
838 provided in the figure legends.
839
840 **Data Availability**
841 The coordinates and structure factors for the $Cpe1_{tox}$–Cpi1 complex have been deposited
842 in the Protein Data Bank, with accession code 9L5U.
843
844
845

Acknowledgments

We thank Drs. Harmit Malik, Dor Salomon, Jun-Yi Leu, Erh-Min Lai, Chih-Horng Kuo, Chih-Yen King, and Ting laboratory members for helpful discussions; Drs. Joseph Mougous, Ming-Yang Ho, Hsin-Hung Chou, and Sue Lin-Chao for sharing reagents; Dr. Hung-Ta Chen for sharing equipment; Drs. Hsin-Nan Lin, Chen-Hsin Yu, Yae-Huei Liou, Sue-Ping Lee, Yung-Hsuan Wu, Shu-Yu Lin, Chuan-Chih Hsu, Chin-Wen Chen, Shu-Chuan Jao, Jin-Hsuan Yu, and Xin-Jie Huang for technical assistance; and Dr. John O'Brien for manuscript editing. We acknowledge funding support from Academia Sinica (AS-CDA-112-L05 to S.-Y.T., AS-IVA-112-L05 to K.-C.H., AS-CDA-110-L01 to C.K., AS-CFII-111-201 to the Academia Sinica Biophysics Core Facility, and AS-CFII-111-209 to the Academia Sinica Common Mass Spectrometry Facilities) and the National Science and Technology Council, Taiwan (111-2311-B-001-006-MY2, 112-2311-B-001-020, and 113-2628-B-001-008-MY3 to S.-Y.T., 112-2320-B-001-006-MY3 to K.-C.H., 111-2611-M001-008-MY3 to C.K., 112-2311-B-001-024-MY3 to the Proteomics Core Lab in the Institute of Plant and Microbial Biology at Academia Sinica).

Competing interests

The authors declare no competing interests.

Figure Legends

Figure 1. PLCP toxins are found in distinct Gram-negative species and are associated with interbacterial toxin delivery pathways. (a) The enzymatic reaction mechanism of papain-like cysteine proteases (PLCPs). The catalytic triad of residues in PLCPs, composed of cysteine (Cys), histidine (His), and aspartate (Asp), facilitates peptide bond cleavage. Histidine and aspartate form

869 a proton-withdrawing group that activates the cysteine residue, converting it into a nucleophile.
870 The activated cysteine attacks the carbonyl carbon of the peptide bond, leading to hydrolysis and
871 bond cleavage. **(b)** Scaled depiction of representative genomic loci from the indicated species
872 (*Edwardsiella tarda*, *Escherichia coli*, *Myxococcales bacterium*, *Roseofilum reptotaenium*,
873 *Citrobacter rodentium*, *Rhizobium* sp., *Burkholderia* sp.) encoding predicted PLCP domain-
874 containing proteins (sky blue) and putative cognate immunity proteins (yellow). Regions encoding
875 N-terminal domains of T6SS-related proteins (PAAR, VgrG, Rhs) are shaded in gray. CDI-related
876 proteins (CdiA, CdiB) are depicted in light brown. Black bars designate locations of bases
877 encoding the catalytic triads of PLCPs. Cysteine residues targeted for mutagenesis in this study
878 are depicted in red. **(c)** Sequence logo generated from alignments of PLCP domains associated
879 with bacterial contact-dependent antagonism pathways (the locus tag numbers for genes encoding
880 the sequences we used are provided in **Supplementary Table 1**). Sequences from previously
881 characterized PLCPs ($ComA_{pep}$ and $LahT_{pep}$) and recently identified T6SS-associated PLCP toxins
882 (EvpQ and TsaP) are shown below for reference. **(d)** Maximum likelihood phylogeny of PLCP
883 effectors visualized as a radiating phylogenetic tree. Taxonomy is indicated by colored shadows,
884 and delivery pathways are indicated by colored tips. The scale bar represents the average number
885 of substitutions per site. See also **Supplementary Figure 2**.
886
887 **Figure 2. $Cpe1_{tox}$-Cpi1 is a functional effector-immunity pair. (a)** Viable *E. coli* cells recovered
888 from plating cultures carrying plasmids expressing the indicated proteins on inducing media. *E.*
889 *coli* carrying plasmid-borne Cpi1 or an empty vector was included to validate suppression of Cpe1
890 toxicity. **(b)** Representative micrographs of *E. coli* cells expressing empty vector, $Cpe1_{tox}$,
891 $Cpe1_{tox}^{C362A}$, or co-expressing $Cpe1_{tox}$ and Cpi1. Frames were acquired 2 hours after induction of

892 protein expression. Scale bar, 2 μm. **(c)** Ribbon diagram representation of the X-ray crystal
893 structure of $Cpe1_{tox}$ (sky blue) in complex with Cpi1 (light gold). Residues of the catalytic triad of
894 $Cpe1_{tox}$ are indicated. **(d)** Structural alignments of $Cpe1_{tox}$ with previously characterized PLCPs:
895 $ComA_{pep}$ (PDB: 3K8U, light gray) and $LahT_{pep}$ (PDB: 6MPZ, dark gray). **(e)** Bacterial competition
896 experiments were conducted on a solid agar over a 6-hour period between the indicated donor and
897 recipient strains. *E. coli* ATCC-11775 Δ*hns* served as the donor strain, whereas *E. coli* MG1655
898 was used as the recipient strain. The Δ*hns* mutation in the donor strain was introduced to upregulate
899 T6SS activity, as described in previous studies[99-101]. **(f)** Depiction of $Cpe1_{tox}$ illustrating the
900 $Cpe1_{tox}$-Cpi1 interaction at the exosite formed by hydrophobic residues. **(g)** Magnified view of the
901 interface between $Cpe1_{tox}$ and Cpi1, highlighting the interacting residues on Cpi1 positioned near
902 the hydrophobic concave surface of $Cpe1_{tox}$. **(h)** Viable *E. coli* cells recovered from *E. coli* co-
903 expressing wild-type $Cpe1_{tox}$ and the indicated Cpi1 variants. **(i)** *In vitro* pull-down assay of
904 $Cpe1_{tox}$ and Cpi1. $Cpe1_{tox}$ proteins were pulled down by strep-tagged Cpi1 variants and
905 immobilized on streptavidin resin. Bound proteins were separated by SDS-PAGE followed by
906 Coomassie brilliant blue staining. Data in **(a)**, **(e)**, and **(h)** are represented as means ± SD. Asterisks
907 indicate significant differences ($p < 0.05$) in viability between populations **(a, h)** or statistically
908 significant differences ($p < 0.05$) between competitive indices of a given donor strain toward the
909 indicated recipients **(e)**. n.s. means no significance. See also **Supplementary Figure 3**,
910 **Supplementary Table 2**, and **Videos 1-4**.
911
912 **Figure 3. $Cpe1_{tox}$ targets and cleaves the type II DNA topoisomerases GyrB and ParE. (a)**
913 Viable *E. coli* cells recovered from expressing $Cpe1_{tox}$ with substitutions of indicated surface
914 residues from the hydrophobic concave region. The expression levels of wild-type and $Cpe1_{tox}$

915 variants were assessed by immunoblotting analysis, using the cytosolic protein RpoB as a loading
916 control (right panel). **(b)** Schematic workflow for identifying candidate substrates of $Cpe1_{tox}$
917 through Bpa crosslinking followed by LC-MS/MS protein identification. Bacteria carrying the
918 construct with a TAG stop codon at residues of interest were grown in medium supplemented with
919 Bpa. After incubation, cells were exposed to long-wavelength UV to activate formation of covalent
920 bonds between Bpa and the interacting residues. Cell lysates were incubated with Ni-NTA resin to
921 enrich for $Cpe1_{tox}$-Bpa crosslinks for further analysis. **(c)** SDS-PAGE gel analysis of crosslinked
922 protein complexes before and after UV_{365nm} treatment. $Cpe1_{tox}^{C362A}$-protein complexes enriched
923 by the Ni-NTA resin were boiled in SDS sample buffer and separated by SDS-PAGE, followed by
924 immunoblotting (α-His). **(d)** Essential proteins identified in the $Cpe1_{tox}^{C362A}$ interactome and their
925 biological functions. The complete interactome dataset is available in **Supplementary Table 3**. **(e,**
926 **f, h, i)** *In vitro* $Cpe1_{tox}$ cleavage assays. Purified $Cpe1_{tox}$ (wild-type or catalytic mutant) were
927 incubated with purified candidate substrates, *i.e.,* GyrB **(e)** and ParE **(f)**, or their variants with
928 single-glycine deletion at the predicted cleavage sites **(h, i)**, to assess hydrolysis by $Cpe1_{tox}$.
929 Fragmented proteins are marked with red arrowheads. Rxn means reaction. **(g)** Double glycine
930 motifs in the consensus regions of *E. coli* GyrB and ParE. Locations of consensus regions between
931 GyrB and ParE containing double glycine motifs are indicated on the cartoon representation of the
932 full-length proteins. The sequences of the consensus regions are shown below, with the positions
933 of the double glycine motifs labeled. The GG motif (red) and the surrounding residues (blue) are
934 highlighted.
935
936 **Figure 4. $Cpe1_{tox}$-mediated intoxication disrupts topoisomerase activity, thereby altering**
937 **DNA topology and impairing DNA replication and chromosome segregation. (a-b)** Ribbon

938 diagrams of *E. coli* GyrB (a, top structure) and ParE (b, top structure) before and after cleavage by
939 $Cpe1_{tox}$. Crystal structures of the 43-kDa ATPase domain of *E. coli* GyrB (PDB: 4PRV) and ParE
940 (PDB: 1S16) were used. Residues of the consensus sequence (LHAGGKF) are shown in yellow.
941 Structure related to the small fragments after $Cpe1_{tox}$ cleavage are indicated as pink ribbons.
942 Predicted structures after cleavage at the double glycine motif demonstrated disruption of the
943 ATPase domain of both GyrB (a, bottom structure) and ParE (b, bottom structure). **(c, d)** Sequence
944 logos evidencing conservation of the consensus sequence (LHAGGKF) of GyrB **(c)** and ParE **(d)**
945 homologs. Cleavage at the double glycine motif is indicated by dashed lines and a scissors
946 illustration. **(e)** Plasmid DNA (pET) was analyzed by high-resolution agarose gel electrophoresis
947 following isolation from *E. coli* that had expressed $Cpe1_{tox}$ or the catalytic mutant for 0.5 or 1 hour.
948 **(f)** *E. coli* cells that had expressed $Cpe1_{tox}$, $Cpe1_{tox}^{C362A}$, or $Cpe1_{tox}$ co-expressed with Cpi1 for
949 three hours. $Cpe1_{tox}$, or the catalytic mutant, was stained with DAPI (DNA; blue) and analyzed by
950 fluorescence microscopy. Phase-contrast (top), blue fluorescence (middle), and merged (bottom)
951 images are presented. Scale bar = 2 μm. Full-size images are available in **Supplementary Figure 7**.
952 **(g)** Working model of how Cpe1 intoxicates bacteria. During interbacterial competition, Cpe1
953 targets and cleaves the ATPase domains of GyrB and ParE in target cells. The cleavage leads to
954 accumulations of unrelaxed supercoils and precatenanes, disrupts DNA segregation, and ultimately
955 inhibits cell division and growth. In the Cpe1-producing cells or kin cells expressing the immunity
956 protein Cpi1, Cpe1 toxicity is neutralized through direct interaction between Cpe1 and Cpi1.
957
958 **Figure 5. Cpi1 employs a competitive inhibitory mechanism to neutralize Cpe1. (a)** The
959 $Cpe1_{tox}$-Cpi1 interface overlaps with the $Cpe1_{tox}$-substrate interaction site. Model predictions of
960 interaction between $Cpe1_{tox}$ and the ATPase domains of GyrB and ParE were constructed using

961 AlphaFold 3. See also **Supplementary Figures 9a, b** for confidence metrics. **(b)** Schematic
962 workflow for the *in vitro* competitive binding assay. Streptavidin resins bound to pre-formed
963 $Cpe1_{tox}^{C362A}$-substrate complexes were prepared and incubated with either wild-type or mutant
964 Cpi1. After incubation, the resins were washed, and the bound proteins were eluted for analysis.
965 Competitive binding events are indicated by disruption of the $Cpe1_{tox}^{C362A}$-substrate interaction,
966 leading to a decreased level of $Cpe1_{tox}^{C362A}$ in the eluted fraction due to its removal during the
967 wash step. **(c, d)** Coomassie-stained SDS-PAGE demonstrating competitive binding events. **(e, f)**
968 Kinetic analysis of interactions between Cpi1 and $Cpe1_{tox}^{C362A}$ **(e)** and $ParE_{ATPase}$ and $Cpe1_{tox}^{C362A}$
969 **(f)** using biolayer interferometry (BLI). Data from three replicates have been plotted on an X-Y
970 scatter graph. The Y-axis represents the wavelength shift generated by binding of the two proteins,
971 normalized to the calculated Rmax (% Rmax) for each run. The X-axis represents reaction time
972 (in seconds). A vertical dashed line marks the transition from the association step to the
973 dissociation step. The mean kinetic parameters (K_d, K_{on}, and K_{off}) and their standard deviations are
974 indicated.
975
976 **Supplementary Figure 1. Interbacterial PLCP effectors and their cognate immunity proteins**
977 **are distributed across various Gram-negative bacteria.** Related to **Figure 1b. (a)** Multiple
978 sequence alignment of 155 unique sequences of interbacterial PLCP effectors. Sequences have
979 been ordered by relative identity to $Cpe1_{tox}$ of *E. coli* ATCC-11775 and are displayed in two
980 clusters divided according to the associated secretion systems (T6SS or CDI). Conserved residues
981 are indicated as follows: the catalytic triad residues are highlighted by red (Cysteine) and orange
982 (Histidine and Aspartate/Asparagine) shadows; and hydrophobic residues composing the surface
983 concave region are highlighted by blue shadows. The Phylum of each strain containing the

984 interbacterial PLCP effectors is indicated by colored boxes (as indicated in the legend). **(b)**
985 Sequences of the putative cognate immunity proteins related to the interbacterial PLCP effectors
986 in **(a)**. Conserved binding residues are highlighted in green shadows. Blank rows indicate an
987 absence of putative immunity proteins due to incomplete genomic data for certain bacterial species
988 in the NCBI database. See also **Supplementary Table 1** for detailed information.
989
990 **Supplementary Figure 2. Interbacterial PLCP effectors exhibit no correlations in phylogeny,**
991 **associated secretion pathways, or taxonomy.** Related to **Figure 1d**. Maximum likelihood
992 phylogeny of 155 unique PLCP effector sequences visualized as a rectangle tree. Branch support
993 values (SH-aLRT and ultrafast bootstrap) are displayed as symbols (filled diamond: SH-aLRT ≥
994 80%, hollow diamonds: ultrafast bootstrap ≥ 95%). Tips representing sequences of the closely-
995 related housekeeping PLCPs, $ComA_{pep}$ and $LahT_{pep}$, as well as the previously identified
996 interbacterial PLCP effectors EvpQ and TsaP, are highlighted in red. The taxonomy of strains
997 containing the PLCP effectors and their associated secretion pathways is indicated on the right as
998 colored boxes. The scale bar represents the average number of substitutions per site. See also
999 **Supplementary Table 1** for detailed information.
1000
1001 **Supplementary Figure 3. Purification of the $Cpe1_{tox}$-Cpi1 complex and protein expression**
1002 **levels of Cpi1 variants.** Related to **Figure 2. (a)** Coomassie-stained SDS-PAGE analysis of the
1003 His-tagged $Cpe1_{tox}$ co-purified with Cpi1. **(b)** Protein expression levels of wild-type Cpi1 and
1004 variants, as assessed by immunoblotting analysis. The cytosolic protein RpoB was used as a
1005 loading control.
1006

1007 **Supplementary Figure 4. $ComA_{pep}$ and $LahT_{pep}$ feature hydrophobic concave regions on**
1008 **their surfaces near the catalytic pocket.** Related to **Figure 3. (a, b)** Depiction of $ComA_{pep}$ **(a)**
1009 and $LahT_{pep}$ **(b)** illustrating the location of their respective catalytic pockets and hydrophobic
1010 concave surfaces. $ComA_{pep}$ (PDB: 3K8U, light gray). $LahT_{pep}$ (PDB: 6MPZ, dark gray).
1011
1012 **Supplementary Figure 5. $Cpe1_{tox}$ specifically targets and cleaves GyrB and ParE among eight**
1013 **candidate substrates identified from the interactome analysis.** Related to **Figure 3. (a-f)**
1014 Coomassie-stained SDS-PAGE analysis of the *in vitro* cleavage assay of six candidate substrates
1015 of $Cpe1_{tox}$: AccA **(a)**, DapE **(b)**, FtsZ **(c)**, NusA **(d)**, NusG **(e)**, and RpoB **(f)**. **(g, h)** Presence of
1016 Cpi1 suppressed the cleavage of GyrB **(g)** and ParE **(h)** by $Cpe1_{tox}$. The substrates were incubated
1017 with $Cpe1_{tox}$ (lanes 1 and 2), $Cpe1_{tox}^{C362A}$ (lanes 3 and 4), or $Cpe1_{tox}$ and Cpi1 (lanes 5 and 6).
1018 Cleaved fragments are indicated with red arrowheads.
1019
1020 **Supplementary Figure 6. Cleavage sequences of ComA and LahT and mass spectrometric**
1021 **analysis of Cpe1-cleaved fragments.** Related to **Figure 4. (a, b)** Sequence logos showing the
1022 consensus sequence recognized by ComA **(a)** and LahT **(b)**. **(c, d)** Mapping of peptide sequences
1023 from $Cpe1_{tox}$-digested GyrB **(c)** and ParE **(d)** fragments. $Cpe1_{tox}$-cleaved fragments, resolved by
1024 Coomassie-stained SDS-PAGE, were purified, trypsin-digested, and subjected to MALDI-TOF
1025 analysis. The intensity of the signals (Y-axis) from identified peptides and their coverage across
1026 the respective full-length protein (X-axis) are plotted below. Upper chart: peptides from the small
1027 fragment. Lower chart: peptides from the large fragment. **(e, f)** Tandem mass spectrum of indicated
1028 peptides from $Cpe1_{tox}$-cleaved GyrB **(e)** and ParE **(g)** fragments. Fragmentation ions (b, blue; y,
1029 red) with resolved spectra and the residues correlating to the LHAGGKF motif (bold) are indicated.

1030 **Supplementary Figure 7. Cpe1 intoxication inhibits chromosome segregation in *E. coli*.**
1031 Related to **Figure 4f. (a)** Phase-contrast (top), blue fluorescence (middle), and merged (bottom)
1032 images of *E. coli* carrying an empty vector, *E. coli* expressing $Cpe1_{tox}$, *E. coli* expressing
1033 $Cpe1_{tox}^{C362A}$, or *E. coli* co-expressing $Cpe1_{tox}$ and Cpi1, after three hours of induction. Scale bar =
1034 20 μm. The white borders demarcate the cropped images displayed in **Figure 4f**.
1035
1036 **Supplementary Figure 8. Z-ring formation is disrupted in Cpe1-intoxicated *E. coli*.** Related
1037 to **Figure 4f. (a)** Phase-contrast (top), blue fluorescence (second from top), green fluorescence
1038 (third from top), and merged (bottom) images of *E. coli* carrying an empty vector, shown before
1039 and after 2-hour incubation. **(b)** Fluorescence micrographs of *E. coli* intoxicated by $Cpe1_{tox}$. Phase-
1040 contrast (top), blue fluorescence (second from top), green fluorescence (third from top), and
1041 merged (bottom) images are presented. White borders indicate the zoomed-in regions shown in the
1042 bottom-right corner of each image. Scale bar = 20 μm.
1043
1044 **Supplementary Figure 9. Interactions between $Cpe1_{tox}$ with the substrates and kinetics of**
1045 **$Cpe1_{tox}$ with $Cpi1^{mut4}$.** Related to **Figures 5 a, e, f. (a, b)** Predicted assigned error (PAE) plots for
1046 the models of the $Cpe1_{tox}$-$GyrB_{ATPase}$ interaction **(a)** and the $Cpe1_{tox}$-$ParE_{ATPase}$ interaction **(b)** in
1047 **Figure 5a**. Accuracy of the predicted relative positions of subunits within the complex, as indicated
1048 by AlphaFold 3 prediction scores (iPTM). Confidence in the overall folding of the complex is
1049 indicated by pTM scores. **(c)** Predicted structure of $Cpe1_{tox}$-$GyrB_{ATPase}$ interaction, showing the
1050 entrance of the consensus loop of GyrB into the active site of Cpe1 (left panel). The magnified
1051 view of the active pocket (right panel) implies possible catalysis. **(d)** $Cpe1_{tox}$ targets the ATPase
1052 domain of ParE. Cleavage of full-length ParE and the ATPase domain by $Cpe1_{tox}$ was analyzed by

1053 Coomassie-stained SDS-PAGE. Cleaved fragments are indicated with red arrowheads. **(e)** Results
1054 of kinetic assays on interactions between $Cpi1^{mut4}$ and $Cpe1_{tox}^{C362A}$ using biolayer interferometry
1055 (BLI). Data from three replicates have been plotted on an X-Y scatter graph. The Y-axis represents
1056 wavelength shift (nm) generated by binding of the two proteins, which is nearly non-detectable
1057 (N.D.). The X-axis represents reaction time in seconds. A vertical dashed line marks the transition
1058 from the association step to the dissociation step. Kinetic parameters such as K_d, K_{on}, K_{off}, and
1059 Rmax could not be calculated and are labeled as ND.
1060
1061 **Video 1. Time-lapse phase contrast microscopy series of *E. coli* containing an empty vector.**
1062 Related to **Figure 2.**
1063 **Video 2. Time-lapse phase contrast microscopy series of *E. coli* expressing $Cpe1_{tox}$.** Related to
1064 **Figure 2.**
1065
1066 **Video 3. Time-lapse phase contrast microscopy series of *E. coli* expressing $Cpe1_{tox}^{C362A}$.**
1067 Related to **Figure 2.**
1068
1069 **Video 4. Time-lapse phase contrast microscopy series of *E. coli* co-expressing $Cpe1_{tox}$ and**
1070 **Cpi1.** Related to **Figure 2.**
1071
1072 **Supplementary Table 1. Identified interbacterial PLCP effectors and their putative cognate**
1073 **immunity proteins.** Relevant to **Figure 1**, **Supplementary Figure 1**, and **Supplementary Figure**
1074 **2**.
1075

1076 **Supplementary Table 2. X-ray data collection and refinement statistics.** Relevant to **Methods**
1077 and **Figure 2**.
1078
1079 **Supplementary Table 3. The interactome of Cpe1 identified by Bpa-crosslinking and LC-**
1080 **MS/MS analysis.** Relevant to **Figure 3**.
1081
1082 **Supplementary Table 4. Strains, recombinant DNA, and oligonucleotides used in this stud**y.
1083

1084 ## Author Contributions

1085 P.-Y.S., C.-E.T., C.K., K.-C.H., and S.-Y.T. designed the study. P.-Y.S., C.-E.T., Y.-C.C., Y.-W.H.,
1086 P.-P.C., T.-H.W., P.-Y.C., and C.-Y.H. performed experiments. P.-Y.S., C.-E.T., P.-P.C., K.-C.H.,
1087 and S.-Y.T. analyzed data. P.-Y.S., C.-E.T., Y.-C.C., P.-P.C., P.-Y.C., K.-C.H., and S.-Y.T. wrote the
1088 manuscript.
1089

1090 ## References

1091 1. Raaijmakers, J.M., and Mazzola, M. (2012). Diversity and natural functions of antibiotics
1092 produced by beneficial and plant pathogenic bacteria. Annu Rev Phytopathol *50*, 403-424.
1093 10.1146/annurev-phyto-081211-172908.
1094 2. Riley, M.A., and Wertz, J.E. (2002). Bacteriocins: evolution, ecology, and application. Annu
1095 Rev Microbiol *56*, 117-137. 10.1146/annurev.micro.56.012302.161024.
1096 3. Aoki, S.K., Pamma, R., Hernday, A.D., Bickham, J.E., Braaten, B.A., and Low, D.A. (2005).
1097 Contact-dependent inhibition of growth in Escherichia coli. Science *309*, 1245-1248.
1098 10.1126/science.1115109.
1099 4. Cao, Z., Casabona, M.G., Kneuper, H., Chalmers, J.D., and Palmer, T. (2016). The type VII
1100 secretion system of Staphylococcus aureus secretes a nuclease toxin that targets
1101 competitor bacteria. Nat Microbiol *2*, 16183. 10.1038/nmicrobiol.2016.183.
1102 5. Hood, R.D., Singh, P., Hsu, F., Guvener, T., Carl, M.A., Trinidad, R.R., Silverman, J.M., Ohlson,
1103 B.B., Hicks, K.G., Plemel, R.L., et al. (2010). A type VI secretion system of Pseudomonas
1104 aeruginosa targets a toxin to bacteria. Cell Host Microbe *7*, 25-37.
1105 10.1016/j.chom.2009.12.007.

1106 6. Jamet, A., Jousset, A.B., Euphrasie, D., Mukorako, P., Boucharlat, A., Ducousso, A., Charbit,
1107 A., and Nassif, X. (2015). A new family of secreted toxins in pathogenic Neisseria species.
1108 PLoS Pathog *11*, e1004592. 10.1371/journal.ppat.1004592.
1109 7. Souza, D.P., Oka, G.U., Alvarez-Martinez, C.E., Bisson-Filho, A.W., Dunger, G., Hobeika, L.,
1110 Cavalcante, N.S., Alegria, M.C., Barbosa, L.R., Salinas, R.K., et al. (2015). Bacterial killing
1111 via a type IV secretion system. Nat Commun *6*, 6453. 10.1038/ncomms7453.
1112 8. Vassallo, C.N., Cao, P., Conklin, A., Finkelstein, H., Hayes, C.S., and Wall, D. (2017).
1113 Infectious polymorphic toxins delivered by outer membrane exchange discriminate kin in
1114 myxobacteria. Elife *6*. 10.7554/eLife.29397.
1115 9. Whitney, J.C., Peterson, S.B., Kim, J., Pazos, M., Verster, A.J., Radey, M.C., Kulasekara, H.D.,
1116 Ching, M.Q., Bullen, N.P., Bryant, D., et al. (2017). A broadly distributed toxin family
1117 mediates contact-dependent antagonism between gram-positive bacteria. Elife *6*.
1118 10.7554/eLife.26938.
1119 10. Sana, T.G., Flaugnatti, N., Lugo, K.A., Lam, L.H., Jacobson, A., Baylot, V., Durand, E., Journet,
1120 L., Cascales, E., and Monack, D.M. (2016). Salmonella Typhimurium utilizes a T6SS-
1121 mediated antibacterial weapon to establish in the host gut. Proc Natl Acad Sci U S A *113*,
1122 E5044-5051. 10.1073/pnas.1608858113.
1123 11. Speare, L., Cecere, A.G., Guckes, K.R., Smith, S., Wollenberg, M.S., Mandel, M.J., Miyashiro,
1124 T., and Septer, A.N. (2018). Bacterial symbionts use a type VI secretion system to eliminate
1125 competitors in their natural host. Proc Natl Acad Sci U S A *115*, E8528-E8537.
1126 10.1073/pnas.1808302115.
1127 12. Verster, A.J., Ross, B.D., Radey, M.C., Bao, Y., Goodman, A.L., Mougous, J.D., and
1128 Borenstein, E. (2017). The Landscape of Type VI Secretion across Human Gut Microbiomes
1129 Reveals Its Role in Community Composition. Cell Host Microbe *22*, 411-419 e414.
1130 10.1016/j.chom.2017.08.010.
1131 13. Russell, A.B., Hood, R.D., Bui, N.K., LeRoux, M., Vollmer, W., and Mougous, J.D. (2011).
1132 Type VI secretion delivers bacteriolytic effectors to target cells. Nature *475*, 343-347.
1133 10.1038/nature10244.
1134 14. Russell, A.B., LeRoux, M., Hathazi, K., Agnello, D.M., Ishikawa, T., Wiggins, P.A., Wai, S.N.,
1135 and Mougous, J.D. (2013). Diverse type VI secretion phospholipases are functionally
1136 plastic antibacterial effectors. Nature *496*, 508-512. 10.1038/nature12074.
1137 15. Fridman, C.M., Keppel, K., Gerlic, M., Bosis, E., and Salomon, D. (2020). A comparative
1138 genomics methodology reveals a widespread family of membrane-disrupting T6SS
1139 effectors. Nat Commun *11*, 1085. 10.1038/s41467-020-14951-4.
1140 16. Sibinelli-Sousa, S., Hespanhol, J.T., Nicastro, G.G., Matsuyama, B.Y., Mesnage, S., Patel, A.,
1141 de Souza, R.F., Guzzo, C.R., and Bayer-Santos, E. (2020). A Family of T6SS Antibacterial
1142 Effectors Related to l,d-Transpeptidases Targets the Peptidoglycan. Cell Rep *31*, 107813.
1143 10.1016/j.celrep.2020.107813.
1144 17. Le, N.H., Pinedo, V., Lopez, J., Cava, F., and Feldman, M.F. (2021). Killing of Gram-negative
1145 and Gram-positive bacteria by a bifunctional cell wall-targeting T6SS effector. Proc Natl
1146 Acad Sci U S A *118*. 10.1073/pnas.2106555118.
1147 18. LaCourse, K.D., Peterson, S.B., Kulasekara, H.D., Radey, M.C., Kim, J., and Mougous, J.D.
1148 (2018). Conditional toxicity and synergy drive diversity among antibacterial effectors. Nat
1149 Microbiol *3*, 440-446. 10.1038/s41564-018-0113-y.

1150 19. Mariano, G., Trunk, K., Williams, D.J., Monlezun, L., Strahl, H., Pitt, S.J., and Coulthurst, S.J.
1151 (2019). A family of Type VI secretion system effector proteins that form ion-selective pores.
1152 Nat Commun *10*, 5484. 10.1038/s41467-019-13439-0.
1153 20. Halvorsen, T.M., Schroeder, K.A., Jones, A.M., Hammarlof, D., Low, D.A., Koskiniemi, S.,
1154 and Hayes, C.S. (2024). Contact-dependent growth inhibition (CDI) systems deploy a large
1155 family of polymorphic ionophoric toxins for inter-bacterial competition. PLoS Genet *20*,
1156 e1011494. 10.1371/journal.pgen.1011494.
1157 21. Ma, L.S., Hachani, A., Lin, J.S., Filloux, A., and Lai, E.M. (2014). Agrobacterium tumefaciens
1158 deploys a superfamily of type VI secretion DNase effectors as weapons for interbacterial
1159 competition in planta. Cell Host Microbe *16*, 94-104. 10.1016/j.chom.2014.06.002.
1160 22. Whitney, J.C., Quentin, D., Sawai, S., LeRoux, M., Harding, B.N., Ledvina, H.E., Tran, B.Q.,
1161 Robinson, H., Goo, Y.A., Goodlett, D.R., et al. (2015). An interbacterial NAD(P)(+)
1162 glycohydrolase toxin requires elongation factor Tu for delivery to target cells. Cell *163*,
1163 607-619. 10.1016/j.cell.2015.09.027.
1164 23. Ahmad, S., Wang, B., Walker, M.D., Tran, H.R., Stogios, P.J., Savchenko, A., Grant, R.A.,
1165 McArthur, A.G., Laub, M.T., and Whitney, J.C. (2019). An interbacterial toxin inhibits target
1166 cell growth by synthesizing (p)ppApp. Nature *575*, 674-678. 10.1038/s41586-019-1735-9.
1167 24. Mok, B.Y., de Moraes, M.H., Zeng, J., Bosch, D.E., Kotrys, A.V., Raguram, A., Hsu, F., Radey,
1168 M.C., Peterson, S.B., Mootha, V.K., et al. (2020). A bacterial cytidine deaminase toxin
1169 enables CRISPR-free mitochondrial base editing. Nature *583*, 631-637. 10.1038/s41586-
1170 020-2477-4.
1171 25. Bullen, N.P., Sychantha, D., Thang, S.S., Culviner, P.H., Rudzite, M., Ahmad, S., Shah, V.S.,
1172 Filloux, A., Prehna, G., and Whitney, J.C. (2022). An ADP-ribosyltransferase toxin kills
1173 bacterial cells by modifying structured non-coding RNAs. Mol Cell *82*, 3484-3498 e3411.
1174 10.1016/j.molcel.2022.08.015.
1175 26. Aoki, S.K., Diner, E.J., de Roodenbeke, C.T., Burgess, B.R., Poole, S.J., Braaten, B.A., Jones,
1176 A.M., Webb, J.S., Hayes, C.S., Cotter, P.A., and Low, D.A. (2010). A widespread family of
1177 polymorphic contact-dependent toxin delivery systems in bacteria. Nature *468*, 439-442.
1178 10.1038/nature09490.
1179 27. Ting, S.Y., Bosch, D.E., Mangiameli, S.M., Radey, M.C., Huang, S., Park, Y.J., Kelly, K.A., Filip,
1180 S.K., Goo, Y.A., Eng, J.K., et al. (2018). Bifunctional Immunity Proteins Protect Bacteria
1181 against FtsZ-Targeting ADP-Ribosylating Toxins. Cell *175*, 1380-1392 e1314.
1182 10.1016/j.cell.2018.09.037.
1183 28. Wang, D., Zhu, L., Zhen, X., Yang, D., Li, C., Chen, Y., Wang, H., Qu, Y., Liu, X., Yin, Y., et al.
1184 (2022). A secreted effector with a dual role as a toxin and as a transcriptional factor. Nat
1185 Commun *13*, 7779. 10.1038/s41467-022-35522-9.
1186 29. Jurenas, D., Rey, M., Byrne, D., Chamot-Rooke, J., Terradot, L., and Cascales, E. (2022).
1187 Salmonella antibacterial Rhs polymorphic toxin inhibits translation through ADP-
1188 ribosylation of EF-Tu P-loop. Nucleic Acids Res *50*, 13114-13127. 10.1093/nar/gkac1162.
1189 30. Dumont, B., Terradot, L., Cascales, E., Van Melderen, L., and Jurenas, D. (2024).
1190 Thioredoxin 1 moonlights as a chaperone for an interbacterial ADP-ribosyltransferase
1191 toxin. Nat Commun *15*, 10388. 10.1038/s41467-024-54892-w.

1192 31. Alcoforado Diniz, J., Liu, Y.C., and Coulthurst, S.J. (2015). Molecular weaponry: diverse
1193 effectors delivered by the Type VI secretion system. Cell Microbiol *17*, 1742-1751.
1194 10.1111/cmi.12532.
1195 32. Bosch, D.E., Abbasian, R., Parajuli, B., Peterson, S.B., and Mougous, J.D. (2023). Structural
1196 disruption of Ntox15 nuclease effector domains by immunity proteins protects against
1197 type VI secretion system intoxication in Bacteroidales. mBio *14*, e0103923.
1198 10.1128/mbio.01039-23.
1199 33. Zhang, D., de Souza, R.F., Anantharaman, V., Iyer, L.M., and Aravind, L. (2012). Polymorphic
1200 toxin systems: Comprehensive characterization of trafficking modes, processing,
1201 mechanisms of action, immunity and ecology using comparative genomics. Biol Direct *7*,
1202 18. 10.1186/1745-6150-7-18.
1203 34. Nachmias, N., Dotan, N., Rocha, M.C., Fraenkel, R., Detert, K., Kluzek, M., Shalom, M.,
1204 Cheskis, S., Peedikayil-Kurien, S., Meitav, G., et al. (2024). Systematic discovery of
1205 antibacterial and antifungal bacterial toxins. Nat Microbiol *9*, 3041-3058.
1206 10.1038/s41564-024-01820-9.
1207 35. Geller, A.M., Shalom, M., Zlotkin, D., Blum, N., and Levy, A. (2024). Identification of type
1208 VI secretion system effector-immunity pairs using structural bioinformatics. Mol Syst Biol
1209 *20*, 702-718. 10.1038/s44320-024-00035-8.
1210 36. Li, D.Y., Liu, Y.L., Liao, X.J., He, T.T., Sun, S.S., Nie, P., and Xie, H.X. (2021). Identification and
1211 Characterization of EvpQ, a Novel T6SS Effector Encoded on a Mobile Genetic Element in
1212 Edwardsiella piscicida. Front Microbiol *12*, 643498. 10.3389/fmicb.2021.643498.
1213 37. Lu, W., Lu, H., Wang, C., Wang, G., Dong, W., and Tan, C. (2023). Effectors of the Type VI
1214 Secretion System Have the Potential to Be Modified into Antimicrobial Peptides. Microbiol
1215 Spectr *11*, e0030823. 10.1128/spectrum.00308-23.
1216 38. Wood, T.E., Howard, S.A., Forster, A., Nolan, L.M., Manoli, E., Bullen, N.P., Yau, H.C.L.,
1217 Hachani, A., Hayward, R.D., Whitney, J.C., et al. (2019). The Pseudomonas aeruginosa T6SS
1218 Delivers a Periplasmic Toxin that Disrupts Bacterial Cell Morphology. Cell Rep *29*, 187-201
1219 e187. 10.1016/j.celrep.2019.08.094.
1220 39. Ashida, H., Sasakawa, C., and Suzuki, T. (2020). A unique bacterial tactic to circumvent the
1221 cell death crosstalk induced by blockade of caspase-8. EMBO J *39*, e104469.
1222 10.15252/embj.2020104469.
1223 40. Gavin, H.E., Beubier, N.T., and Satchell, K.J. (2017). The Effector Domain Region of the
1224 Vibrio vulnificus MARTX Toxin Confers Biphasic Epithelial Barrier Disruption and Is
1225 Essential for Systemic Spread from the Intestine. PLoS Pathog *13*, e1006119.
1226 10.1371/journal.ppat.1006119.
1227 41. Kitadokoro, K., Kamitani, S., Miyazawa, M., Hanajima-Ozawa, M., Fukui, A., Miyake, M.,
1228 and Horiguchi, Y. (2007). Crystal structures reveal a thiol protease-like catalytic triad in the
1229 C-terminal region of Pasteurella multocida toxin. Proc Natl Acad Sci U S A *104*, 5139-5144.
1230 10.1073/pnas.0608197104.
1231 42. Havarstein, L.S., Diep, D.B., and Nes, I.F. (1995). A family of bacteriocin ABC transporters
1232 carry out proteolytic processing of their substrates concomitant with export. Mol
1233 Microbiol *16*, 229-240. 10.1111/j.1365-2958.1995.tb02295.x.
1234 43. Kanonenberg, K., Spitz, O., Erenburg, I.N., Beer, T., and Schmitt, L. (2018). Type I secretion
1235 system-it takes three and a substrate. FEMS Microbiol Lett *365*. 10.1093/femsle/fny094.

1236 44. Kieuvongngam, V., Olinares, P.D.B., Palillo, A., Oldham, M.L., Chait, B.T., and Chen, J. (2020).
1237 Structural basis of substrate recognition by a polypeptide processing and secretion
1238 transporter. Elife *9*. 10.7554/eLife.51492.
1239 45. Altschul, S.F., Madden, T.L., Schaffer, A.A., Zhang, J., Zhang, Z., Miller, W., and Lipman, D.J.
1240 (1997). Gapped BLAST and PSI-BLAST: a new generation of protein database search
1241 programs. Nucleic Acids Res *25*, 3389-3402. 10.1093/nar/25.17.3389.
1242 46. Jurenas, D., and Journet, L. (2021). Activity, delivery, and diversity of Type VI secretion
1243 effectors. Mol Microbiol *115*, 383-394. 10.1111/mmi.14648.
1244 47. Gunther, P., Quentin, D., Ahmad, S., Sachar, K., Gatsogiannis, C., Whitney, J.C., and Raunser,
1245 S. (2022). Structure of a bacterial Rhs effector exported by the type VI secretion system.
1246 PLoS Pathog *18*, e1010182. 10.1371/journal.ppat.1010182.
1247 48. Klein, T.A., Ahmad, S., and Whitney, J.C. (2020). Contact-Dependent Interbacterial
1248 Antagonism Mediated by Protein Secretion Machines. Trends Microbiol *28*, 387-400.
1249 10.1016/j.tim.2020.01.003.
1250 49. Ishii, S., Yano, T., and Hayashi, H. (2006). Expression and characterization of the peptidase
1251 domain of Streptococcus pneumoniae ComA, a bifunctional ATP-binding cassette
1252 transporter involved in quorum sensing pathway. J Biol Chem *281*, 4726-4731.
1253 10.1074/jbc.M512516200.
1254 50. Bobeica, S.C., Dong, S.H., Huo, L., Mazo, N., McLaughlin, M.I., Jimenez-Oses, G., Nair, S.K.,
1255 and van der Donk, W.A. (2019). Insights into AMS/PCAT transporters from biochemical and
1256 structural characterization of a double Glycine motif protease. Elife *8*.
1257 10.7554/eLife.42305.
1258 51. Ozhelvaci, F., and Steczkiewicz, K. (2023). Identification and classification of papain-like
1259 cysteine proteinases. J Biol Chem *299*, 104801. 10.1016/j.jbc.2023.104801.
1260 52. Ishii, S., Yano, T., Ebihara, A., Okamoto, A., Manzoku, M., and Hayashi, H. (2010). Crystal
1261 structure of the peptidase domain of Streptococcus ComA, a bifunctional ATP-binding
1262 cassette transporter involved in the quorum-sensing pathway. J Biol Chem *285*, 10777-
1263 10785. 10.1074/jbc.M109.093781.
1264 53. Holm, L. (2022). Dali server: structural unification of protein families. Nucleic Acids Res *50*,
1265 W210-W215. 10.1093/nar/gkac387.
1266 54. Ishii, S., Fukui, K., Yokoshima, S., Kumagai, K., Beniyama, Y., Kodama, T., Fukuyama, T.,
1267 Okabe, T., Nagano, T., Kojima, H., and Yano, T. (2017). High-throughput Screening of Small
1268 Molecule Inhibitors of the Streptococcus Quorum-sensing Signal Pathway. Sci Rep *7*, 4029.
1269 10.1038/s41598-017-03567-2.
1270 55. Chin, J.W., Martin, A.B., King, D.S., Wang, L., and Schultz, P.G. (2002). Addition of a
1271 photocrosslinking amino acid to the genetic code of Escherichiacoli. Proc Natl Acad Sci U
1272 S A *99*, 11020-11024. 10.1073/pnas.172226299.
1273 56. Kauer, J.C., Erickson-Viitanen, S., Wolfe, H.R., Jr., and DeGrado, W.F. (1986). p-Benzoyl-L-
1274 phenylalanine, a new photoreactive amino acid. Photolabeling of calmodulin with a
1275 synthetic calmodulin-binding peptide. J Biol Chem *261*, 10695-10700.
1276 57. Karp, P.D., Weaver, D., Paley, S., Fulcher, C., Kubo, A., Kothari, A., Krummenacker, M.,
1277 Subhraveti, P., Weerasinghe, D., Gama-Castro, S., et al. (2014). The EcoCyc Database.
1278 EcoSal Plus *6*. 10.1128/ecosalplus.ESP-0009-2013.

1279 58. Baba, T., Ara, T., Hasegawa, M., Takai, Y., Okumura, Y., Baba, M., Datsenko, K.A., Tomita,
1280 M., Wanner, B.L., and Mori, H. (2006). Construction of Escherichia coli K-12 in-frame,
1281 single-gene knockout mutants: the Keio collection. Mol Syst Biol *2*, 2006 0008.
1282 10.1038/msb4100050.
1283 59. Havarstein, L.S., Holo, H., and Nes, I.F. (1994). The leader peptide of colicin V shares
1284 consensus sequences with leader peptides that are common among peptide bacteriocins
1285 produced by gram-positive bacteria. Microbiology (Reading) *140 (Pt 9)*, 2383-2389.
1286 10.1099/13500872-140-9-2383.
1287 60. Kotake, Y., Ishii, S., Yano, T., Katsuoka, Y., and Hayashi, H. (2008). Substrate recognition
1288 mechanism of the peptidase domain of the quorum-sensing-signal-producing ABC
1289 transporter ComA from Streptococcus. Biochemistry *47*, 2531-2538. 10.1021/bi702253n.
1290 61. Levine, C., Hiasa, H., and Marians, K.J. (1998). DNA gyrase and topoisomerase IV:
1291 biochemical activities, physiological roles during chromosome replication, and drug
1292 sensitivities. Biochim Biophys Acta *1400*, 29-43. 10.1016/s0167-4781(98)00126-2.
1293 62. Bush, N.G., Evans-Roberts, K., and Maxwell, A. (2015). DNA Topoisomerases. EcoSal Plus
1294 *6*. 10.1128/ecosalplus.ESP-0010-2014.
1295 63. Wang, J.C. (2002). Cellular roles of DNA topoisomerases: a molecular perspective. Nat Rev
1296 Mol Cell Biol *3*, 430-440. 10.1038/nrm831.
1297 64. Drlica, K., and Zhao, X. (1997). DNA gyrase, topoisomerase IV, and the 4-quinolones.
1298 Microbiol Mol Biol Rev *61*, 377-392. 10.1128/mmbr.61.3.377-392.1997.
1299 65. Azam, M.A., Thathan, J., and Jubie, S. (2015). Dual targeting DNA gyrase B (GyrB) and
1300 topoisomerse IV (ParE) inhibitors: A review. Bioorg Chem *62*, 41-63.
1301 10.1016/j.bioorg.2015.07.004.
1302 66. Vanden Broeck, A., Lotz, C., Ortiz, J., and Lamour, V. (2019). Cryo-EM structure of the
1303 complete E. coli DNA gyrase nucleoprotein complex. Nat Commun *10*, 4935.
1304 10.1038/s41467-019-12914-y.
1305 67. Bellon, S., Parsons, J.D., Wei, Y., Hayakawa, K., Swenson, L.L., Charifson, P.S., Lippke, J.A.,
1306 Aldape, R., and Gross, C.H. (2004). Crystal structures of Escherichia coli topoisomerase IV
1307 ParE subunit (24 and 43 kilodaltons): a single residue dictates differences in novobiocin
1308 potency against topoisomerase IV and DNA gyrase. Antimicrob Agents Chemother *48*,
1309 1856-1864. 10.1128/AAC.48.5.1856-1864.2004.
1310 68. Caron, P.R., and Wang, J.C. (1994). Appendix. II: Alignment of primary sequences of DNA
1311 topoisomerases. Adv Pharmacol *29B*, 271-297. 10.1016/s1054-3589(08)61143-6.
1312 69. O'Dea, M.H., Tamura, J.K., and Gellert, M. (1996). Mutations in the B subunit of
1313 Escherichia coli DNA gyrase that affect ATP-dependent reactions. J Biol Chem *271*, 9723-
1314 9729. 10.1074/jbc.271.16.9723.
1315 70. Lamour, V., Hoermann, L., Jeltsch, J.M., Oudet, P., and Moras, D. (2002). An open
1316 conformation of the Thermus thermophilus gyrase B ATP-binding domain. J Biol Chem *277*,
1317 18947-18953. 10.1074/jbc.M111740200.
1318 71. Clark, D.J., and Leblanc, B. (2009). Analysis of DNA supercoiling induced by DNA-protein
1319 interactions. Methods Mol Biol *543*, 523-535. 10.1007/978-1-60327-015-1_30.
1320 72. Lockshon, D., and Morris, D.R. (1983). Positively supercoiled plasmid DNA is produced by
1321 treatment of Escherichia coli with DNA gyrase inhibitors. Nucleic Acids Res *11*, 2999-3017.
1322 10.1093/nar/11.10.2999.

1323 73. Mossessova, E., Levine, C., Peng, H., Nurse, P., Bahng, S., and Marians, K.J. (2000).
1324 Mutational analysis of Escherichia coli topoisomerase IV. I. Selection of dominant-negative
1325 parE alleles. J Biol Chem *275*, 4099-4103. 10.1074/jbc.275.6.4099.
1326 74. Kato, J., Nishimura, Y., Imamura, R., Niki, H., Hiraga, S., and Suzuki, H. (1990). New
1327 topoisomerase essential for chromosome segregation in E. coli. Cell *63*, 393-404.
1328 10.1016/0092-8674(90)90172-b.
1329 75. Smith, D.H., and Davis, B.D. (1967). Mode of action of novobiocin in Escherichia coli. J
1330 Bacteriol *93*, 71-79. 10.1128/jb.93.1.71-79.1967.
1331 76. Ouyang, X., Hoeksma, J., Lubbers, R.J.M., Siersma, T.K., Hamoen, L.W., and den Hertog, J.
1332 (2022). Classification of antimicrobial mechanism of action using dynamic bacterial
1333 morphology imaging. Sci Rep *12*, 11162. 10.1038/s41598-022-15405-1.
1334 77. Moore, D.A., Whatley, Z.N., Joshi, C.P., Osawa, M., and Erickson, H.P. (2017). Probing for
1335 Binding Regions of the FtsZ Protein Surface through Site-Directed Insertions: Discovery of
1336 Fully Functional FtsZ-Fluorescent Proteins. J Bacteriol *199*. 10.1128/JB.00553-16.
1337 78. Abramson, J., Adler, J., Dunger, J., Evans, R., Green, T., Pritzel, A., Ronneberger, O.,
1338 Willmore, L., Ballard, A.J., Bambrick, J., et al. (2024). Accurate structure prediction of
1339 biomolecular interactions with AlphaFold 3. Nature *630*, 493-500. 10.1038/s41586-024-
1340 07487-w.
1341 79. Shao, F., Merritt, P.M., Bao, Z., Innes, R.W., and Dixon, J.E. (2002). A Yersinia effector and a
1342 Pseudomonas avirulence protein define a family of cysteine proteases functioning in
1343 bacterial pathogenesis. Cell *109*, 575-588. 10.1016/s0092-8674(02)00766-3.
1344 80. Shao, F., Golstein, C., Ade, J., Stoutemyer, M., Dixon, J.E., and Innes, R.W. (2003). Cleavage
1345 of Arabidopsis PBS1 by a bacterial type III effector. Science *301*, 1230-1233.
1346 10.1126/science.1085671.
1347 81. Kourelis, J., van der Hoorn, R.A.L., and Sueldo, D.J. (2016). Decoy Engineering: The Next
1348 Step in Resistance Breeding. Trends Plant Sci *21*, 371-373. 10.1016/j.tplants.2016.04.001.
1349 82. Noeske-Jungblut, C., Haendler, B., Donner, P., Alagon, A., Possani, L., and Schleuning, W.D.
1350 (1995). Triabin, a highly potent exosite inhibitor of thrombin. J Biol Chem *270*, 28629-
1351 28634. 10.1074/jbc.270.48.28629.
1352 83. Fuentes-Prior, P., Noeske-Jungblut, C., Donner, P., Schleuning, W.D., Huber, R., and Bode,
1353 W. (1997). Structure of the thrombin complex with triabin, a lipocalin-like exosite-binding
1354 inhibitor derived from a triatomine bug. Proc Natl Acad Sci U S A *94*, 11845-11850.
1355 10.1073/pnas.94.22.11845.
1356 84. Hanna, R.A., Campbell, R.L., and Davies, P.L. (2008). Calcium-bound structure of calpain
1357 and its mechanism of inhibition by calpastatin. Nature *456*, 409-412.
1358 10.1038/nature07451.
1359 85. Moldoveanu, T., Gehring, K., and Green, D.R. (2008). Concerted multi-pronged attack by
1360 calpastatin to occlude the catalytic cleft of heterodimeric calpains. Nature *456*, 404-408.
1361 10.1038/nature07353.
1362 86. Kleanthous, C., and Walker, D. (2001). Immunity proteins: enzyme inhibitors that avoid the
1363 active site. Trends Biochem Sci *26*, 624-631. 10.1016/s0968-0004(01)01941-7.
1364 87. Schiavo, G., and van der Goot, F.G. (2001). The bacterial toxin toolkit. Nat Rev Mol Cell Biol
1365 *2*, 530-537. 10.1038/35080089.

88. Schiavo, G., Benfenati, F., Poulain, B., Rossetto, O., Polverino de Laureto, P., DasGupta, B.R., and Montecucco, C. (1992). Tetanus and botulinum-B neurotoxins block neurotransmitter release by proteolytic cleavage of synaptobrevin. Nature *359*, 832-835. 10.1038/359832a0.
89. Sutormin, D.A., Galivondzhyan, A.K., Polkhovskiy, A.V., Kamalyan, S.O., Severinov, K.V., and Dubiley, S.A. (2021). Diversity and Functions of Type II Topoisomerases. Acta Naturae *13*, 59-75. 10.32607/actanaturae.11058.
90. Wang, J., Chitsaz, F., Derbyshire, M.K., Gonzales, N.R., Gwadz, M., Lu, S., Marchler, G.H., Song, J.S., Thanki, N., Yamashita, R.A., et al. (2023). The conserved domain database in 2023. Nucleic Acids Res *51*, D384-D388. 10.1093/nar/gkac1096.
91. Journet, L., and Cascales, E. (2016). The Type VI Secretion System in Escherichia coli and Related Species. EcoSal Plus *7*. 10.1128/ecosalplus.ESP-0009-2015.
92. Jones, A.M., Low, D.A., and Hayes, C.S. (2017). Can't you hear me knocking: contact-dependent competition and cooperation in bacteria. Emerg Top Life Sci *1*, 75-83. 10.1042/ETLS20160019.
93. Thompson, J.D., Higgins, D.G., and Gibson, T.J. (1994). CLUSTAL W: improving the sensitivity of progressive multiple sequence alignment through sequence weighting, position-specific gap penalties and weight matrix choice. Nucleic Acids Res *22*, 4673-4680. 10.1093/nar/22.22.4673.
94. Trifinopoulos, J., Nguyen, L.T., von Haeseler, A., and Minh, B.Q. (2016). W-IQ-TREE: a fast online phylogenetic tool for maximum likelihood analysis. Nucleic Acids Res *44*, W232-235. 10.1093/nar/gkw256.
95. Edwards, R.A., Keller, L.H., and Schifferli, D.M. (1998). Improved allelic exchange vectors and their use to analyze 987P fimbria gene expression. Gene *207*, 149-157. 10.1016/s0378-1119(97)00619-7.
96. Gibson, D.G., Young, L., Chuang, R.Y., Venter, J.C., Hutchison, C.A., 3rd, and Smith, H.O. (2009). Enzymatic assembly of DNA molecules up to several hundred kilobases. Nat Methods *6*, 343-345. 10.1038/nmeth.1318.
97. Choi, K.H., Gaynor, J.B., White, K.G., Lopez, C., Bosio, C.M., Karkhoff-Schweizer, R.R., and Schweizer, H.P. (2005). A Tn7-based broad-range bacterial cloning and expression system. Nat Methods *2*, 443-448. 10.1038/nmeth765.
98. Gross, C.H., Parsons, J.D., Grossman, T.H., Charifson, P.S., Bellon, S., Jernee, J., Dwyer, M., Chambers, S.P., Markland, W., Botfield, M., and Raybuck, S.A. (2003). Active-site residues of Escherichia coli DNA gyrase required in coupling ATP hydrolysis to DNA supercoiling and amino acid substitutions leading to novobiocin resistance. Antimicrob Agents Chemother *47*, 1037-1046. 10.1128/AAC.47.3.1037-1046.2003.
99. Wan, B., Zhang, Q., Ni, J., Li, S., Wen, D., Li, J., Xiao, H., He, P., Ou, H.Y., Tao, J., et al. (2017). Type VI secretion system contributes to Enterohemorrhagic Escherichia coli virulence by secreting catalase against host reactive oxygen species (ROS). PLoS Pathog *13*, e1006246. 10.1371/journal.ppat.1006246.
100. Brunet, Y.R., Khodr, A., Logger, L., Aussel, L., Mignot, T., Rimsky, S., and Cascales, E. (2015). H-NS Silencing of the Salmonella Pathogenicity Island 6-Encoded Type VI Secretion System Limits Salmonella enterica Serovar Typhimurium Interbacterial Killing. Infect Immun *83*, 2738-2750. 10.1128/IAI.00198-15.

1410 101. Serapio-Palacios, A., Woodward, S.E., Vogt, S.L., Deng, W., Creus-Cuadros, A., Huus, K.E.,
1411 Cirstea, M., Gerrie, M., Barcik, W., Yu, H., and Finlay, B.B. (2022). Type VI secretion systems
1412 of pathogenic and commensal bacteria mediate niche occupancy in the gut. Cell Rep *39*,
1413 110731. 10.1016/j.celrep.2022.110731.
1414 102. Otwinowski, Z., and Minor, W. (1997). Processing of X-ray diffraction data collected in
1415 oscillation mode. Methods Enzymol *276*, 307-326. 10.1016/S0076-6879(97)76066-X.
1416 103. Adams, P.D., Afonine, P.V., Bunkoczi, G., Chen, V.B., Davis, I.W., Echols, N., Headd, J.J., Hung,
1417 L.W., Kapral, G.J., Grosse-Kunstleve, R.W., et al. (2010). PHENIX: a comprehensive Python-
1418 based system for macromolecular structure solution. Acta Crystallogr D Biol Crystallogr *66*,
1419 213-221. 10.1107/S0907444909052925.
1420 104. Emsley, P., and Cowtan, K. (2004). Coot: model-building tools for molecular graphics. Acta
1421 Crystallogr D Biol Crystallogr *60*, 2126-2132. 10.1107/S0907444904019158.
1422 105. Ryu, Y., and Schultz, P.G. (2006). Efficient incorporation of unnatural amino acids into
1423 proteins in Escherichia coli. Nat Methods *3*, 263-265. 10.1038/nmeth864.
1424 106. Cox, J., and Mann, M. (2008). MaxQuant enables high peptide identification rates,
1425 individualized p.p.b.-range mass accuracies and proteome-wide protein quantification.
1426 Nat Biotechnol *26*, 1367-1372. 10.1038/nbt.1511.
1427 107. Tyanova, S., Mann, M., and Cox, J. (2014). MaxQuant for in-depth analysis of large SILAC
1428 datasets. Methods Mol Biol *1188*, 351-364. 10.1007/978-1-4939-1142-4_24.
1429 108. Shevchenko, A., Tomas, H., Havlis, J., Olsen, J.V., and Mann, M. (2006). In-gel digestion for
1430 mass spectrometric characterization of proteins and proteomes. Nat Protoc *1*, 2856-2860.
1431 10.1038/nprot.2006.468.
1432 109. Liu, Y., Hua, Z.C., and Leng, F. (2018). DNA Supercoiling Measurement in Bacteria. Methods
1433 Mol Biol *1703*, 63-73. 10.1007/978-1-4939-7459-7_4.
1434 110. UniProt, C. (2023). UniProt: the Universal Protein Knowledgebase in 2023. Nucleic Acids
1435 Res *51*, D523-D531. 10.1093/nar/gkac1052.
1436 111. Crooks, G.E., Hon, G., Chandonia, J.M., and Brenner, S.E. (2004). WebLogo: a sequence
1437 logo generator. Genome Res *14*, 1188-1190. 10.1101/gr.849004.
1438

Figure 1

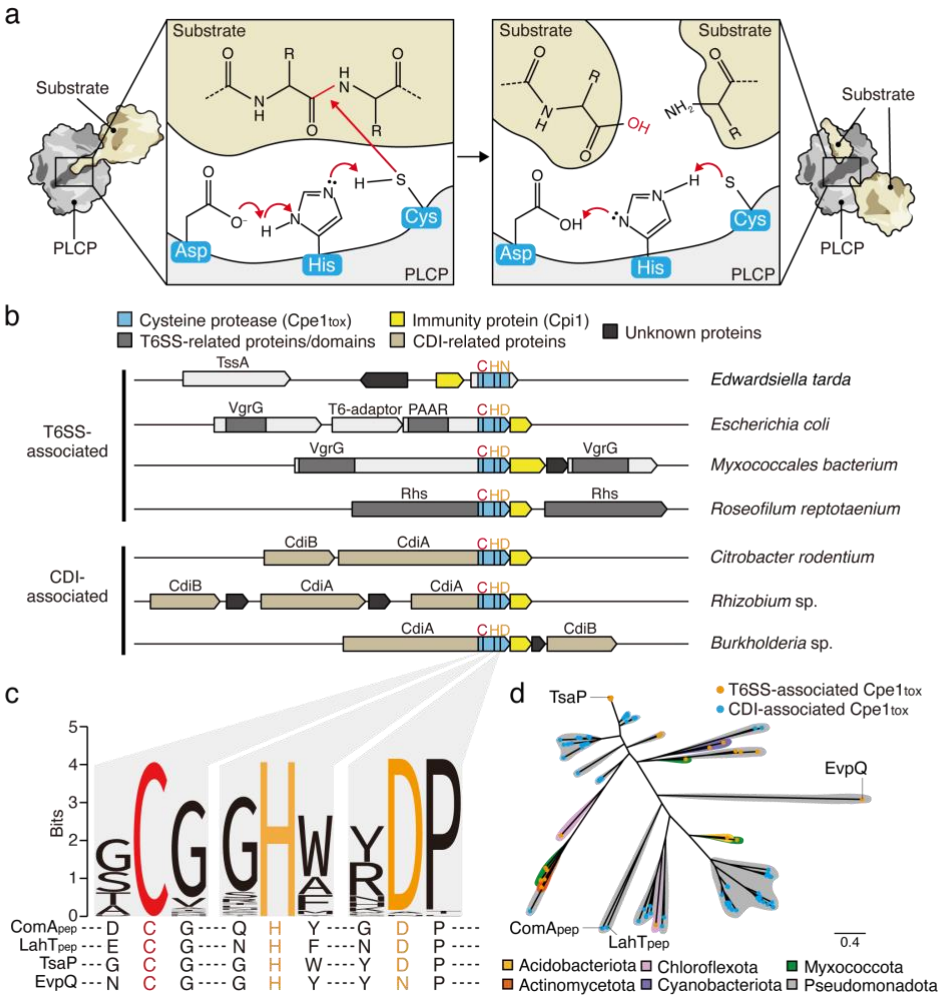

Figure 1. PLCP toxins are found in distinct Gram-negative species and are associated with interbacterial toxin delivery pathways. (a) The enzymatic reaction mechanism of papain-like cysteine proteases (PLCPs). The catalytic triad of residues in PLCPs, composed of cysteine (Cys), histidine (His), and aspartate (Asp), facilitates peptide bond cleavage. Histidine and aspartate form a proton-withdrawing group that activates the cysteine residue, converting it into a nucleophile. The activated cysteine attacks the carbonyl carbon of the peptide bond, leading to hydrolysis and bond cleavage. **(b)** Scaled depiction of representative genomic loci from the indicated species (*Edwardsiella tarda*, *Escherichia coli*, *Myxococcales bacterium*, *Roseofilum reptotaenium*, *Citrobacter rodentium*, *Rhizobium* sp., *Burkholderia* sp.) encoding predicted PLCP domain-containing proteins (sky blue) and putative cognate immunity proteins (yellow). Regions encoding N-terminal domains of T6SS-related proteins (PAAR, VgrG, Rhs) are shaded in gray. CDI-related proteins (CdiA, CdiB) are depicted in light brown. Black bars designate locations of bases encoding the catalytic triads of PLCPs. Cysteine residues targeted for mutagenesis in this study are depicted in red. **(c)** Sequence logo generated from alignments of PLCP domains associated with bacterial contact-dependent antagonism pathways (the locus tag numbers for genes encoding the sequences we used are provided in **Supplementary Table 1**). Sequences from previously characterized PLCPs ($ComA_{pep}$ and $LahT_{pep}$) and recently identified T6SS-associated PLCP toxins (EvpQ and TsaP) are shown below for reference. **(d)** Maximum likelihood phylogeny of PLCP effectors visualized as a radiating phylogenetic tree. Taxonomy is indicated by colored shadows, and delivery pathways are indicated by colored tips. The scale bar represents the average number of substitutions per site. See also **Supplementary Figure 2**.

Figure 2

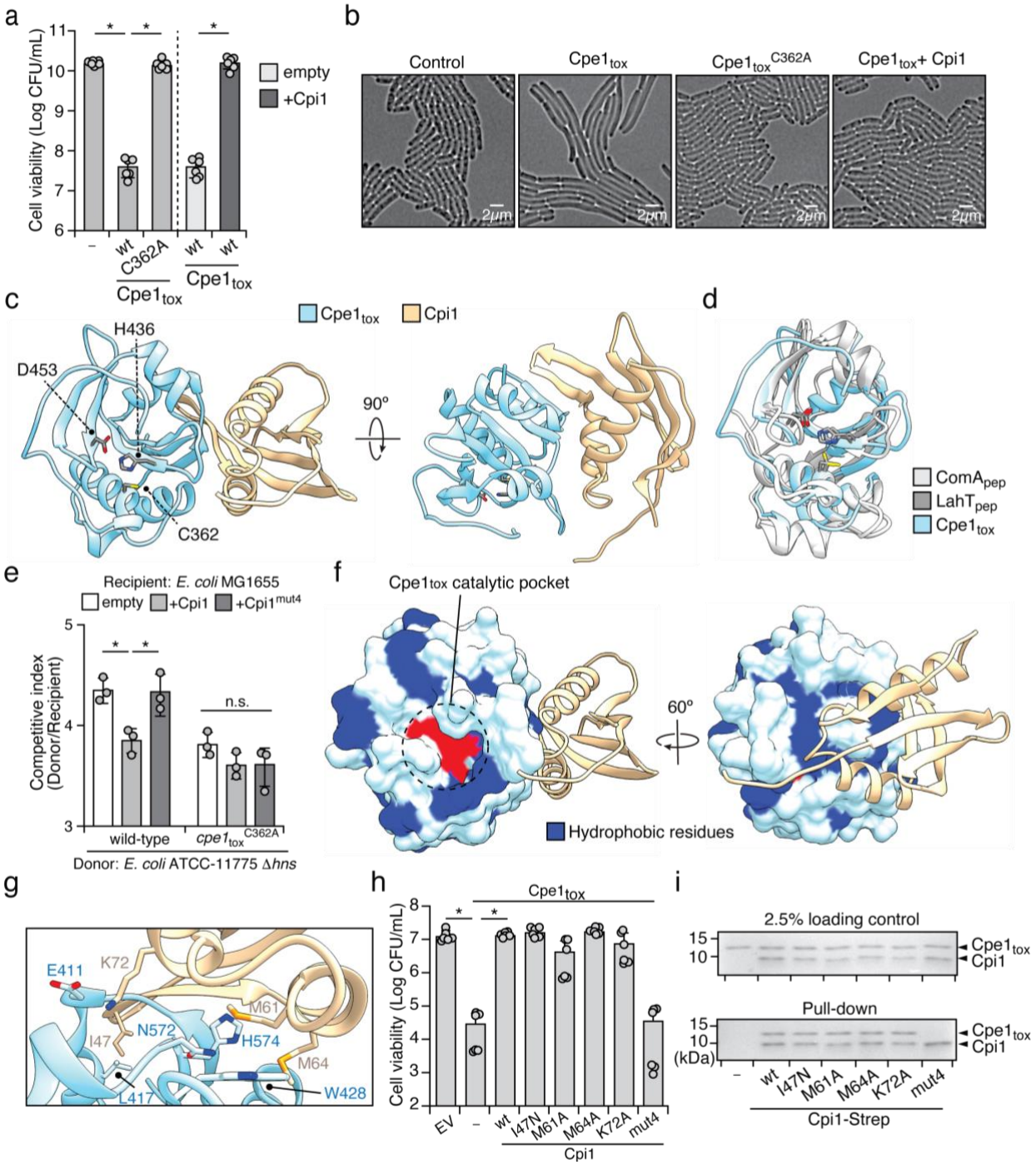

Figure 2. $Cpe1_{tox}$-Cpi1 is a functional effector-immunity pair. (a) Viable *E. coli* cells recovered from plating cultures carrying plasmids expressing the indicated proteins on inducing media. *E. coli* carrying plasmid-borne Cpi1 or an empty vector was included to validate suppression of Cpe1 toxicity. **(b)** Representative micrographs of *E. coli* cells expressing empty vector, $Cpe1_{tox}$, $Cpe1_{tox}^{C362A}$, or co-expressing $Cpe1_{tox}$ and Cpi1. Frames were acquired 2 hours after induction of protein expression. Scale bar, 2 μm. **(c)** Ribbon diagram representation of the X-ray crystal structure of $Cpe1_{tox}$ (sky blue) in complex with Cpi1 (light gold). Residues of the catalytic triad of $Cpe1_{tox}$ are indicated. **(d)** Structural alignments of $Cpe1_{tox}$ with previously characterized PLCPs: $ComA_{pep}$ (PDB: 3K8U, light gray) and $LahT_{pep}$ (PDB: 6MPZ, dark gray). **(e)** Bacterial competition experiments were conducted on a solid agar over a 6-hour period between the indicated donor and recipient strains. *E. coli* ATCC-11775 Δ*hns* served as the donor strain, whereas *E. coli* MG1655 was used as the recipient strain. The Δ*hns* mutation in the donor strain was introduced to upregulate T6SS activity, as described in previous studies[99-101]. **(f)** Depiction of $Cpe1_{tox}$ illustrating the $Cpe1_{tox}$-Cpi1 interaction at the exosite formed by hydrophobic residues. **(g)** Magnified view of the interface between $Cpe1_{tox}$ and Cpi1, highlighting the interacting residues on Cpi1 positioned near the hydrophobic concave surface of $Cpe1_{tox}$. **(h)** Viable *E. coli* cells recovered from *E. coli* co-expressing wild-type $Cpe1_{tox}$ and the indicated Cpi1 variants. **(i)** *In vitro* pull-down assay of $Cpe1_{tox}$ and Cpi1. $Cpe1_{tox}$ proteins were pulled down by strep-tagged Cpi1 variants and immobilized on streptavidin resin. Bound proteins were separated by SDS-PAGE followed by Coomassie brilliant blue staining. Data in **(a)**, **(e)**, and **(h)** are represented as means ± SD. Asterisks indicate significant differences ($p < 0.05$) in viability between populations **(a, h)** or statistically significant differences ($p < 0.05$) between competitive indices of a given donor strain toward the indicated recipients **(e)**. n.s. means no significance. See also **Supplementary Figure 3**, **Supplementary Table 2**, and **Videos 1-4**.

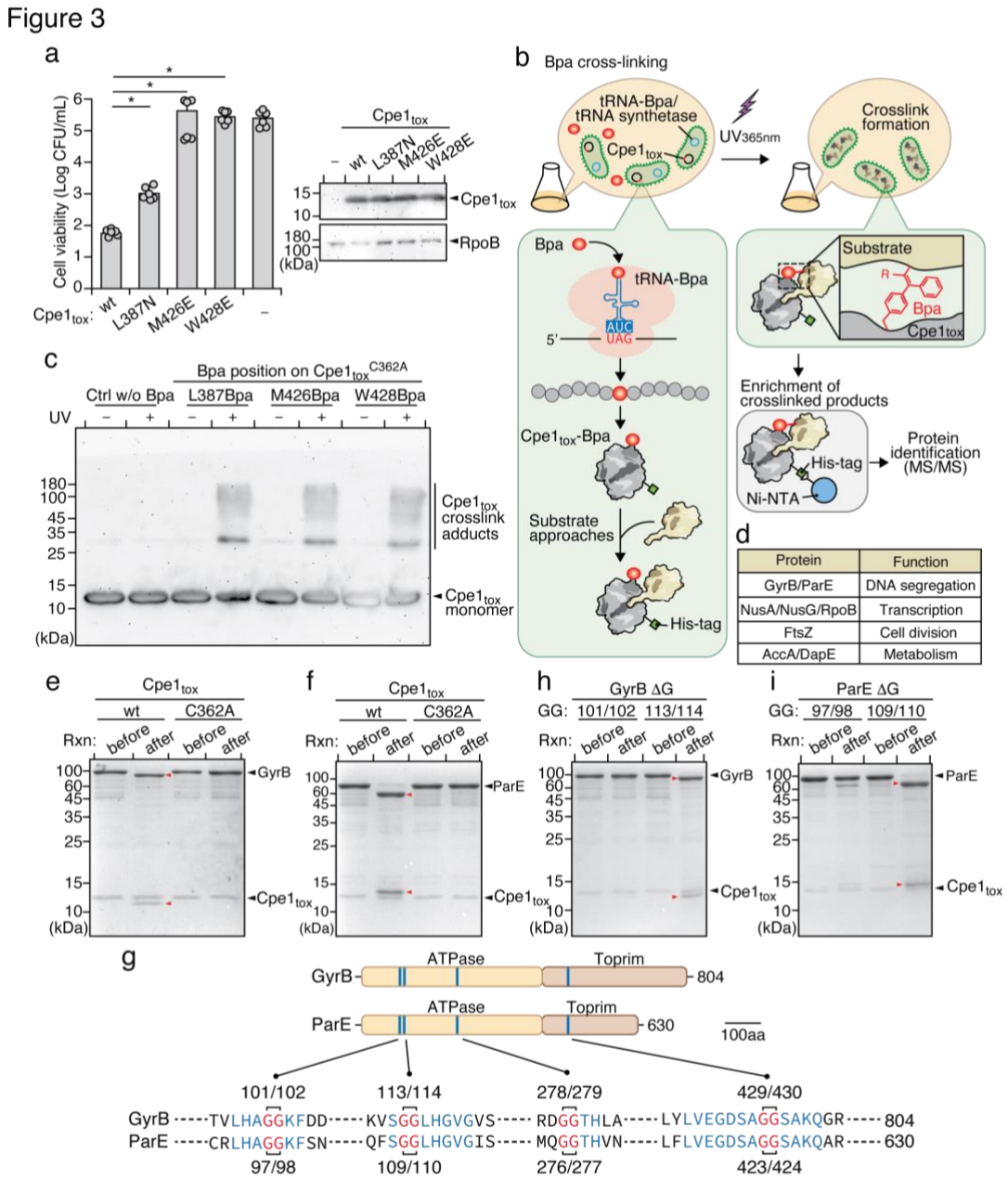

Figure 3. Cpe1$_{tox}$ targets and cleaves the type II DNA topoisomerases GyrB and ParE. (a) Viable *E. coli* cells recovered from expressing Cpe1$_{tox}$ with substitutions of indicated surface residues from the hydrophobic concave region. The expression levels of wild-type and Cpe1$_{tox}$ variants were assessed by immunoblotting analysis, using the cytosolic protein RpoB as a loading control (right panel). **(b)** Schematic workflow for identifying candidate substrates of Cpe1$_{tox}$ through Bpa crosslinking followed by LC-MS/MS protein identification. Bacteria carrying the construct with a TAG stop codon at residues of interest were grown in medium supplemented with Bpa. After incubation, cells were exposed to long-wavelength UV to activate formation of covalent bonds between Bpa and the interacting residues. Cell lysates were incubated with Ni-NTA resin to enrich for Cpe1$_{tox}$-Bpa crosslinks for further analysis. **(c)** SDS-PAGE gel analysis of crosslinked protein complexes before and after UV$_{365nm}$ treatment. Cpe1$_{tox}^{C362A}$-protein complexes enriched by the Ni-NTA resin were boiled in SDS sample buffer and separated by SDS-PAGE, followed by immunoblotting (α-His). **(d)** Essential proteins identified in the Cpe1$_{tox}^{C362A}$ interactome and their biological functions. The complete interactome dataset is available in **Supplementary Table 3**. **(e, f, h, i)** *In vitro* Cpe1$_{tox}$ cleavage assays. Purified Cpe1$_{tox}$ (wild-type or catalytic mutant) were incubated with purified candidate substrates, *i.e.,* GyrB **(e)** and ParE **(f)**, or their variants with single-glycine deletion at the predicted cleavage sites **(h, i)**, to assess hydrolysis by Cpe1$_{tox}$. Fragmented proteins are marked with red arrowheads. Rxn means reaction. **(g)** Double glycine motifs in the consensus regions of *E. coli* GyrB and ParE. Locations of consensus regions between GyrB and ParE containing double glycine motifs are indicated on the cartoon representation of the full-length proteins. The sequences of the consensus regions are shown below, with the positions of the double glycine motifs labeled. The GG motif (red) and the surrounding residues (blue) are highlighted.

Figure 4

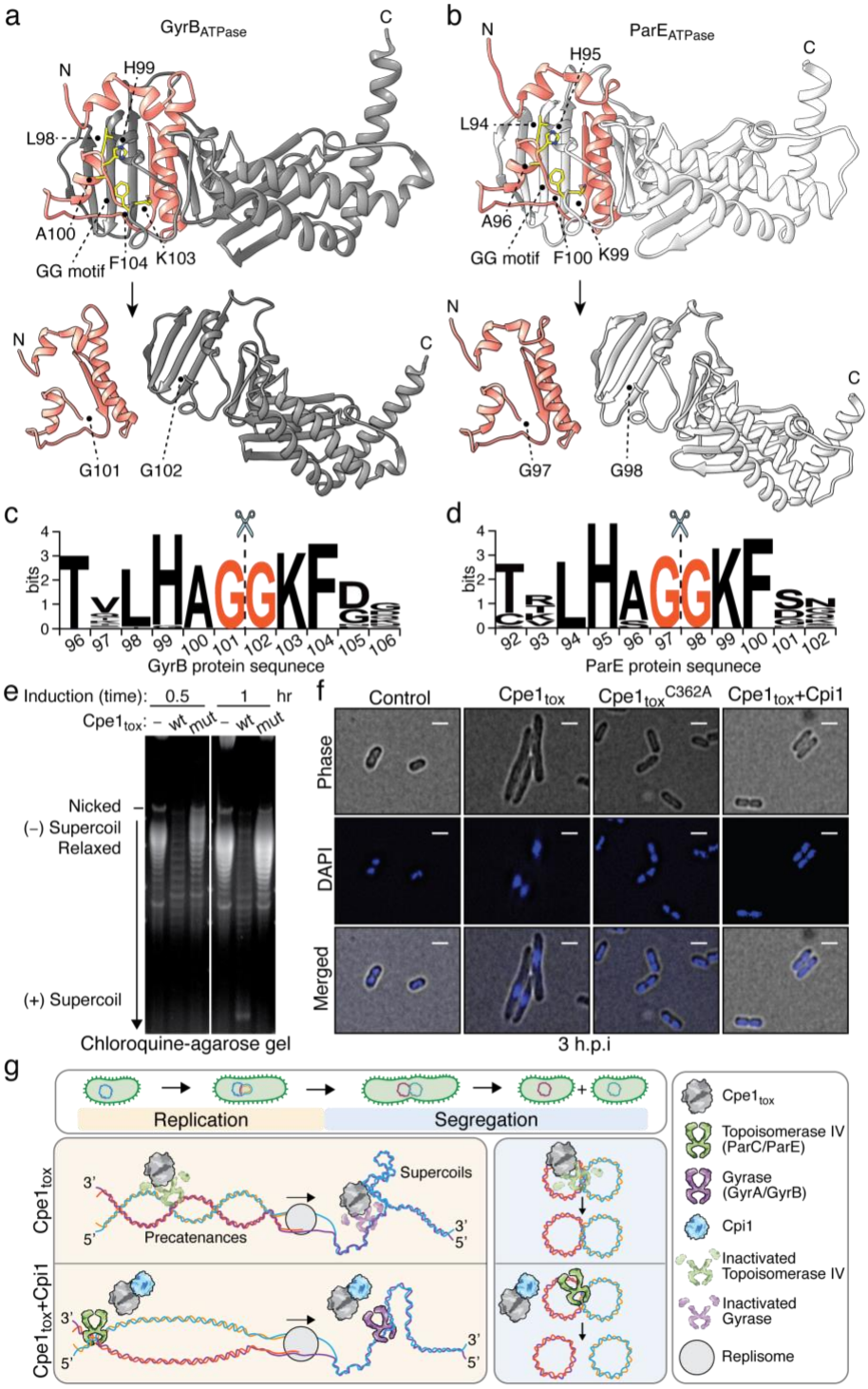

Figure 4. Cpe1$_{tox}$-mediated intoxication disrupts topoisomerase activity, thereby altering DNA topology and impairing DNA replication and chromosome segregation. (a-b) Ribbon diagrams of *E. coli* GyrB (a, top structure) and ParE (b, top structure) before and after cleavage by Cpe1$_{tox}$. Crystal structures of the 43-kDa ATPase domain of *E. coli* GyrB (PDB: 4PRV) and ParE (PDB: 1S16) were used. Residues of the consensus sequence (LHAGGKF) are shown in yellow. Structure related to the small fragments after Cpe1$_{tox}$ cleavage are indicated as pink ribbons. Predicted structures after cleavage at the double glycine motif demonstrated disruption of the ATPase domain of both GyrB (a, bottom structure) and ParE (b, bottom structure). **(c, d)** Sequence logos evidencing conservation of the consensus sequence (LHAGGKF) of GyrB **(c)** and ParE **(d)** homologs. Cleavage at the double glycine motif is indicated by dashed lines and a scissors illustration. **(e)** Plasmid DNA (pET) was analyzed by high-resolution agarose gel electrophoresis following isolation from *E. coli* that had expressed Cpe1$_{tox}$ or the catalytic mutant for 0.5 or 1 hour. **(f)** *E. coli* cells that had expressed Cpe1$_{tox}$, Cpe1$_{tox}$^{C362A}, or Cpe1$_{tox}$ co-expressed with Cpi1 for three hours. Cpe1$_{tox}$, or the catalytic mutant, was stained with DAPI (DNA; blue) and analyzed by fluorescence microscopy. Phase-contrast (top), blue fluorescence (middle), and merged (bottom) images are presented. Scale bar = 2 µm. Full-size images are available in **Supplementary Figure 7**. **(g)** Working model of how Cpe1 intoxicates bacteria. During interbacterial competition, Cpe1 targets and cleaves the ATPase domains of GyrB and ParE in target cells. The cleavage leads to accumulations of unrelaxed supercoils and precatenanes, disrupts DNA segregation, and ultimately inhibits cell division and growth. In the Cpe1-producing cells or kin cells expressing the immunity protein Cpi1, Cpe1 toxicity is neutralized through direct interaction between Cpe1 and Cpi1.

Figure 5

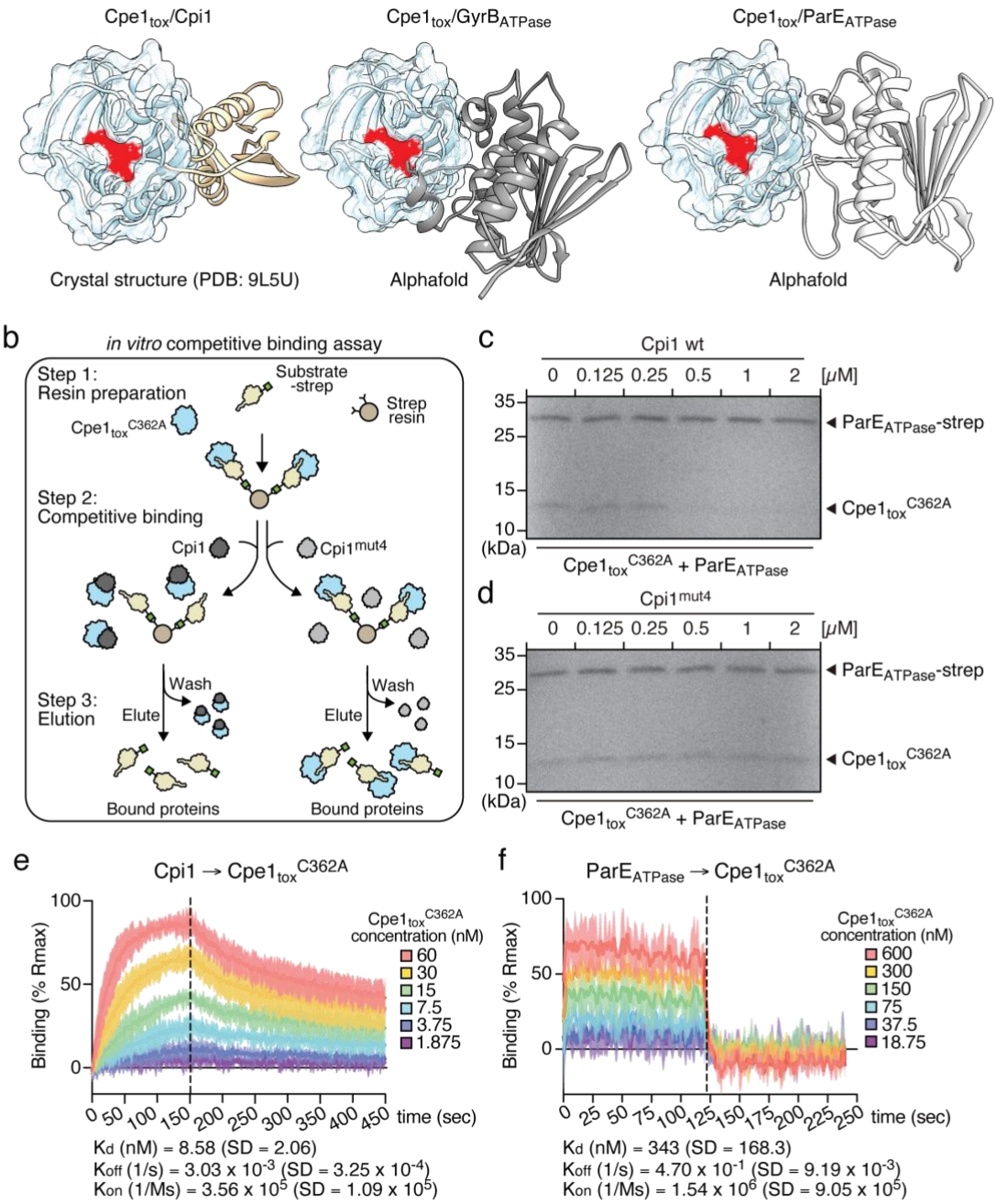

Figure 5. Cpi1 employs a competitive inhibitory mechanism to neutralize Cpe1. (a) The $Cpe1_{tox}$-Cpi1 interface overlaps with the $Cpe1_{tox}$-substrate interaction site. Model predictions of interaction between $Cpe1_{tox}$ and the ATPase domains of GyrB and ParE were constructed using AlphaFold 3. See also **Supplementary Figures 9a, b** for confidence metrics. **(b)** Schematic workflow for the *in vitro* competitive binding assay. Streptavidin resins bound to pre-formed $Cpe1_{tox}^{C362A}$-substrate complexes were prepared and incubated with either wild-type or mutant Cpi1. After incubation, the resins were washed, and the bound proteins were eluted for analysis. Competitive binding events are indicated by disruption of the $Cpe1_{tox}^{C362A}$-substrate interaction, leading to a decreased level of $Cpe1_{tox}^{C362A}$ in the eluted fraction due to its removal during the wash step. **(c, d)** Coomassie-stained SDS-PAGE demonstrating competitive binding events. **(e, f)** Kinetic analysis of interactions between Cpi1 and $Cpe1_{tox}^{C362A}$ **(e)** and $ParE_{ATPase}$ and $Cpe1_{tox}^{C362A}$ **(f)** using biolayer interferometry (BLI). Data from three replicates have been plotted on an X-Y scatter graph. The Y-axis represents the wavelength shift generated by binding of the two proteins, normalized to the calculated Rmax (% Rmax) for each run. The X-axis represents reaction time (in seconds). A vertical dashed line marks the transition from the association step to the dissociation step. The mean kinetic parameters (K_d, K_{on}, and K_{off}) and their standard deviations are indicated.